Beauty Production in Z decays

Gary Taylor

Thesis submitted for the degree of Doctor of Philosophy
of the University of London
and the Diploma of Membership of Imperial College.

January 1991

Imperial College
London

Abstract

The fraction of $b\bar{b}$ events produced in hadronic Z decays has been studied using inclusive lepton production in data collected by the ALEPH detector at LEP. With around 1.17 pb^{-1} of integrated luminosity, corresponding to about 25,000 hadronic Z decays, the $b\bar{b}$ fraction times the semileptonic branching ratio was measured to be $(\Gamma(Z \rightarrow b\bar{b})/\Gamma(Z \rightarrow q\bar{q})).Br(b \rightarrow l) = 0.0206 \pm 0.0016(stat) \pm 0.0016(syst)$. Assuming a value of 0.103 ± 0.010 for the average semileptonic branching ratio gives $\Gamma(Z \rightarrow b\bar{b})/\Gamma(Z \rightarrow q\bar{q}) = 0.200 \pm 0.016(stat) \pm 0.026(syst)$ in good agreement with the Standard Model prediction of 0.217.

Acknowledgements

I have enjoyed these last three years, both at Imperial College, working under Professor Binnie, and at CERN. I am very grateful to Dr William Cameron, my supervisor, for the help and encouragement I received throughout the three years. I thank Dr Peter Dornan, the head of the ALEPH group at Imperial College, for directing me through the important stages of my analysis. I gratefully acknowledge the financial support of the British public provided under the auspices of the Science and Engineering Research Council.

I would like to thank all the people with whom I collaborated whilst working on ALEPH. I enjoyed being involved with the commissioning of the ALEPH data acquisition system and working with Marco and the Online Group (Wolfgang, Tim, John, Pere, Condor, Beat, Sandro, Andy and Julian). My analysis would not have been possible without the efforts of Georgio, Roberto, Pierluigi, Fabio and Luca who provided most of the basic tools I used for muon identification. I would like to thank Ray, without his help the preparation of this thesis would have taken significantly longer.

For their diligent proof reading of this thesis I am heavily indebted to Bill, Carol, Dan, Ian and John.

Away from work I enjoyed being in the company of Steve, Tad, Robbo, Martin, Gary "again", Pete-like, Simon, Matty, Mark, Tony, Andy, Dan, Aileen, Elaine, Julia, Helen, Jill, Sarah and Michelle who helped to keep me sane (well almost). I "doth the proverbial cap" to Affie for being Affie better than almost anyone else I know. Special thanks to Aileen for giving me some of my fondest memories.

The Author's Contribution

I joined the ALEPH group at Imperial College in September 1987. The group's contribution to the ALEPH experiment, the Inner Tracking Chamber, had already been built and had performed well in test-beam studies carried out in the summer of that year. My initial involvement was the debugging and commissioning of the ITC R-Φ Trigger Processor. This involved writing a large software simulation package which was used to diagnose hardware faults. After the hardware was fully debugged I wrote a set of computer programs to allow a non-expert to control remotely the operation of the processor. This work is briefly discussed in section 3.1.4.

In parallel with this I took responsibility for testing and overhauling the TDCs used for both z and r-ϕ coordinate measurement. This led naturally onto the writing of the data acquisition tasks to perform the initialization and readout of the ITC electronics. These tasks were subsequently adapted to fit into the framework of the central ALEPH data acquisition system. The ITC was the first subdetector to be fully integrated in this way. It was therefore used to test and commission the data acquisition system as a whole and I was heavily involved with this process. Although this work was an extremely important contribution to the successful operation of the ALEPH detector it has not been discussed in this thesis.

When ALEPH was successfully taking data I became involved with the heavy flavour analysis. At the time this group was primarily working on a measurement of the heavy flavour production cross-sections in Z decays, obtained by studying inclusive lepton production. My contribution to this analysis was to study the efficiency and backgrounds associated with the selection of inclusive muon candidates. The results I obtained were used in the relevant ALEPH publication [1]. For this thesis the analysis was repeated essentially unchanged using a more recent, and much improved, processing of the same data sample. The Monte Carlo simulation used for this thesis was tuned to reproduce ALEPH data, while that used for the paper had been generated before LEP was operational. I have also redone the inclusive electron analysis presented in the paper with the reprocessed data set. In the electron case I essentially repeated the analysis outlined in the paper (which was not my work) but I have made some changes

where I thought they were necessary and also carried out some more cross-checks. I also looked in more detail at various sources of systematic error.

To my father and mother,

George and Elizabeth.

Contents

List of Figures

List of Tables

Chapter 1

Introduction

1.1 The Standard Model

The two basic aims of elementary particle physics are the identification of the structureless constituents of matter and the explanation of the nature of the fundamental forces acting between them. At present there are thought to be only four fundamental forces; corresponding to the gravitational, electromagnetic, strong nuclear and weak nuclear interactions. There are, on the other hand, more than twenty particles which are currently believed to be elementary, and each of these has its corresponding antiparticle. These can be categorized into two distinct types, *matter* particles and *force carrying* particles. The matter particles have half-integral spins (fermions), whilst the force carrying particles have integral spins (bosons). The matter particles may be further categorized into quarks (which experience the strong nuclear force) and leptons (which do not). These quarks and leptons can be grouped into three generations of weak isospin doublets giving for the quarks,

$$\begin{pmatrix} u \\ d' \end{pmatrix} \qquad \begin{pmatrix} c \\ s' \end{pmatrix} \qquad \begin{pmatrix} t \\ b' \end{pmatrix}$$

and for the leptons,

$$\begin{pmatrix} \nu_e \\ e^- \end{pmatrix} \qquad \begin{pmatrix} \nu_\mu \\ \mu^- \end{pmatrix} \qquad \begin{pmatrix} \nu_\tau \\ \tau^- \end{pmatrix}$$

where the generations are arranged in order of increasing mass. The $'$ above the d, s, b quarks denotes the fact that they are weak eigenstates. These can be related to the mass eigenstates by the Cabbibo-Kobayashi-Maskawa (CKM) [2] matrix. Of all the particles in the above doublets only the top (t) quark and the tau neutrino (ν_τ) have still to be experimentally observed.

Of the four known forces, gravity has a negligible effect in determining the behaviour of elementary particles. The current theoretical description of the other three forces is embodied in a set of three quantum field theories which together form the Standard Model. In these theories the force between any two fermions is thought to be mediated by the exchange of a boson. The equations of motion describing the free fermionic fields are required to satisfy the Dirac [3] equation. In quantum field theory these equations of motion may be derived from a free field Lagrangian. The nature of the interaction between the fermionic fields is then determined by requiring the corresponding Lagrangian to be invariant under local gauge transformations belonging to a given symmetry group.

In the Standard Model the electromagnetic and weak nuclear forces are unified. They are thought to be different manifestations of the same fundamental force, the electroweak force. The symmetry group associated with this force is $SU(2)_L \otimes U(1)_Y$ [1]. The invariance of the Lagrangian under the local gauge transformations belonging to this group requires the introduction of four new quantum fields; the quanta of which are the $\gamma, W^\pm$ and Z bosons. Moreover this invariance requirement completely determines the form of the interactions between these gauge bosons and the fermions, and even between the gauge bosons themselves. The symmetry of the electroweak theory is seen, experimentally, to be broken in a way which gives mass to the $W^\pm$ and Z while keeping the photon massless. Theoretically this *spontaneous symmetry breaking* can be accommodated by the introduction of another particle, the Higgs boson [4]. There is, as yet, no experimental evidence confirming the existence of such a particle.

Of the leptons only the quarks are observed to experience the strong nuclear force.

[1] The L subscript denotes the fact that only left-handed fermions are observed to take part in charged weak interactions. The Y subscript is used to emphasize that the $U(1)$ symmetry corresponds to weak hypercharge and not electromagnetic charge.

There is strong experimental evidence [5] that each flavour of quark (u, d, s, c, b, t) carries a hidden degree of freedom known as colour. This colour degree of freedom can take one of three possible values. The strong force is believed to couple only to coloured objects. The symmetry group associated with the strong force is $SU(3)_C$ and the associated quantum field theory is known as Quantum Chromodynamics (QCD). Invariance under local $SU(3)_C$ transformations requires the introduction of another 8 bosonic quantum fields carrying the colour degree of freedom, the gluons.

1.2 The Z Boson

In their work on electroweak unification Glashow, Salam, and Weinberg [6,7,8] suggested that there should exist a neutral weak current, mediated by the Z boson, to partner the two experimentally observed charged weak currents. Testing this hypothesis experimentally was a difficult task since in almost all low energy processes the effects of any weak neutral current would be masked by the much stronger electromagnetic current. Indeed it was not until 1973 that the first experimental evidence for such a process was obtained [9]. It came in the form of a bubble chamber photograph of the reaction $\bar{\nu_\mu} e^- \rightarrow \bar{\nu_\mu} e^-$. The subsequent discovery of the $W^\pm$ and Z bosons in 1983 [10,11] provided striking confirmation of the predictive power of the unified electroweak theory.

Within the framework of this theory the Z boson can be produced in e^+e^- annihilations, before subsequently decaying into fermion-antifermion pairs. The amplitude for this process can be calculated from the relevant Feynman diagram [12] shown in figure 1.1.

In the Born approximation, the width for the Z to decay into a given fermion-antifermion pair is given by [13],

$$\Gamma_B(Z \rightarrow f\bar{f}) = \beta(\frac{3-\beta^2}{2})\Gamma_0^V + \beta^3\Gamma_0^A$$

with,

$$\Gamma_0^{V(A)} = \frac{G_\mu m_Z^3}{24\sqrt{2}\pi} v_f^2(a_f^2)$$

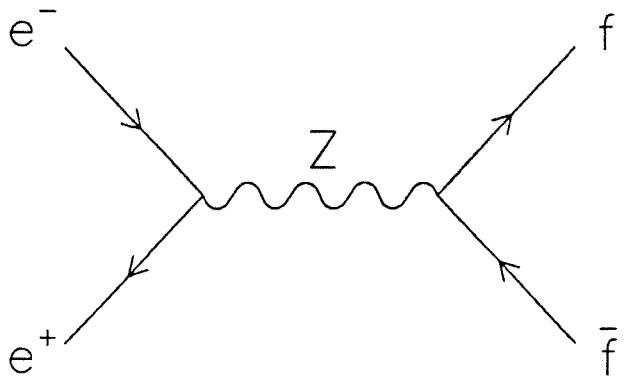

Figure 1.1: *Feynman diagram for fermion-antifermion pair production in Z decays.*

The electroweak vector and axial couplings are given as,

$$v_f = 2t_3 - 4Q_f \sin^2\theta_W \ , \ a_f = 2t_3$$

where the third component of weak isospin (t_3) and charge (Q_f) are given in table 1.1 for the different fermion types. The Weinberg angle (θ_W) reflects the extent to which the weak and electromagnetic currents mix. Its magnitude is not predicted by the electroweak theory but $\sin^2\theta_W$ has been measured to be 0.229 $\pm$0.004 [14]. The widths for massless fermion-antifermion pair production in the Born approximation, including the quark colour factor, are given in table 1.1. Kinematic effects due to non-zero fermion masses enter through the β term,

$$\beta = \sqrt{1 - \frac{4m_f^2}{s}}$$

where m_f is the fermion mass and s is the square of the centre of mass energy.

The Born approximation widths must be corrected to take into account the effect of higher order processes. The QED corrections, which come mainly from the effect of final state radiation, are negligible. QCD corrections, known up to second order for massless quarks, increase each of the quark partial widths by approximately 3%. This correction is independent of quark flavour. When quark mass effects are taken into account, to first order, the QCD correction to the $b\bar{b}$ width is enhanced by a further 0.5%.

Fermion Type	t_3	Q_f	$\Gamma_B(\mathrm{MeV/c^2})$
ν_e, ν_μ, ν_τ	+1/2	0	162
e^-, μ^-, τ^-	−1/2	-1	81
u,c	+1/2	+2/3	280
d,s,b	−1/2	−1/3	360

Table 1.1: *Third component of weak hypercharge, charge, and Z decay width, in the Born approximation, for different fermion types.*

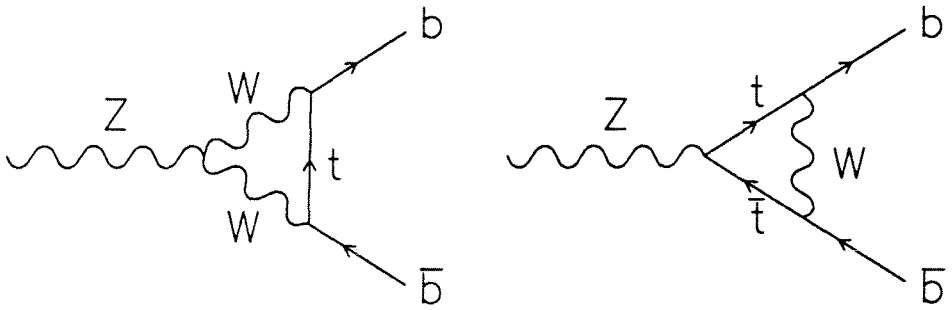

Figure 1.2: *Examples of electroweak vertex corrections involving top quarks.*

In the case of electroweak corrections there are certain vertex diagrams involving top quarks which only contribute significantly to the $b\bar{b}$ width[2], see figure 1.2. This leads to a variation of the ratio $\Gamma(Z \to b\bar{b})/\Gamma(Z \to q\bar{q})$ with top quark mass as shown in figure 1.3. This variation is much stronger than that induced by a reasonable variation in the Higgs mass. With the above corrections included, the Standard Model prediction[3] for the ratio $\Gamma_B(Z \to b\bar{b})/\Gamma_B(Z \to q\bar{q})$ is 0.217.

This thesis describes a measurement of this partial width. It was obtained using inclusive lepton tagging to select an enriched sample of $b\bar{b}$ events. Before describing how this is done in detail it is necessary to discuss some general features of hadronic

[2]This is because the top and beauty quarks belong to the same weak isospin doublet. Transitions between them are therefore not CKM suppressed.

[3]For $M_Z = 91.18\,\mathrm{GeV/c^2}$ [14], $\alpha_s = 0.12$ [15], $M_{top} = 150\,\mathrm{GeV/c^2}$, $M_{Higgs} = 100\,\mathrm{GeV/c^2}$.

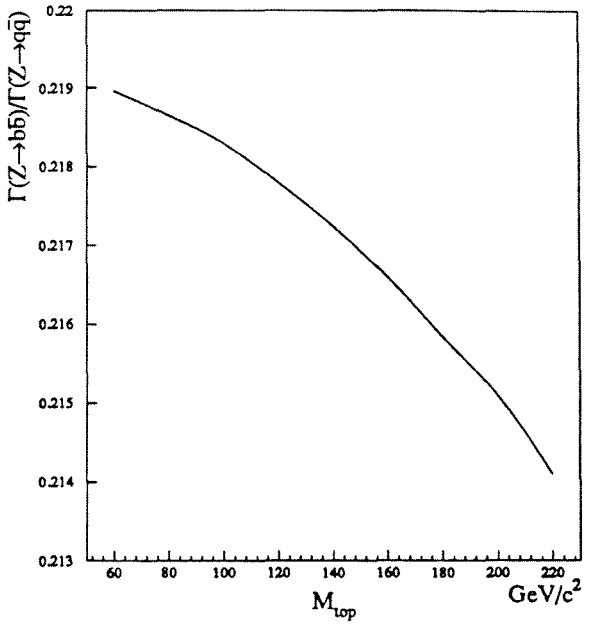

Figure 1.3: *Variation of* $\Gamma(Z \rightarrow b\bar{b})/\Gamma(Z \rightarrow q\bar{q})$ *with top quark mass.*

events and the uncertainties inherent in their Monte Carlo simulation.

1.3 Hadronic Event Structure

The underlying structure of hadronic events is believed to be determined by the properties of the strong nuclear force. At low momentum transfers (large distances) the force between two coloured objects is observed to be very strong. The strength of the force in this energy region is believed to be responsible for the *confinement* of coloured quarks into colour singlet hadrons. There are two known types of hadrons: mesons, made from a quark-antiquark (colour-anticolour) pair, and baryons made from three quarks, one of each colour. Vacuum polarization effects are thought to lead to a decrease in the effective coupling at higher momentum transfers (shorter distances); a phenomenon known as *asymptotic freedom.*

The momentum transfer associated with Z decays is quite large and perturbation theory can therefore be used to predict the relative rates of production of events with differing numbers of final state partons (quarks and gluons). These rates have, as yet, only been calculated to second order in perturbation theory. Second order calculations

lead to final states with at most four partons. There is experimental evidence [15] that, at the momentum transfers in question, processes involving five or more final state partons cannot be neglected.

As the partons move apart the strength of the colour force between them increases. The corresponding increase in the stored energy of the parton-parton system allows the production of further $q\bar{q}$ pairs from the vacuum. In most of the phenomenological models available this fragmentation process stops when the stored energy falls below some preset threshold. At this stage neighbouring quarks and antiquarks are combined appropriately to form colour singlet hadrons. The details of these processes, which occur in the region of strong coupling, cannot be calculated using perturbation theory. It is these hadrons, and their decay products, which are observed by particle detectors. The observed hadrons appear to be collimated in a small number of jets, groups of particles which were initially travelling in a similar direction. Each jet is, in general, thought to correspond to the fragmentation of a single energetic parton.

1.4 Hadronic Event Simulation

For the analysis presented in this thesis the simulation of hadronic events was performed using the JETSET 6.3 [16] software package. The JETSET package has been shown to provide a good description of the properties of hadronic events over a wide range of centre of mass energies [15,17]. The important parameters of the program were tuned to reproduce a variety of global event shape and single particle distributions observed in hadronic decays at LEP energies [15]. Where necessary, minor modifications were made to include the effects of initial and final state photon radiation and substantial improvements were made to the particle decay schemes used.

The simulation of hadronic events [18] can be pictured as taking place in several distinct stages as shown in figure 1.4. In stage (i) the e^+e^- annihilate to form a Z (or a photon) which subsequently decays into a $q\bar{q}$ pair. It is possible for either the initial state leptons or the final state quarks to radiate a photon. In practise this is implemented by an appropriate interfacing of the JETSET package with the dimuon event generator DYMU2 [19].

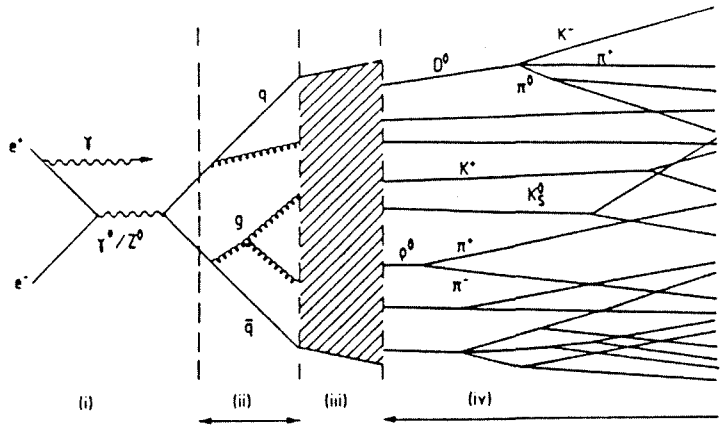

Figure 1.4: *The various steps involved in the simulation of an e^+e^- annihilation event.*

In stage (ii) the $q\bar{q}$ pair produced are allowed to radiate gluons which may subsequently produce new $q\bar{q}$ pairs or further gluons. In this way events with differing numbers of final state partons may be obtained. Matrix element techniques should, in principle, give the best description of this process. There are, however, discrepancies between data and Monte Carlos based on second order matrix elements. These discrepancies are thought to be caused by the lack of third and higher order diagrams. To overcome these deficiencies a *parton shower* model is used, in which successive splittings of the type $q \rightarrow qg$, $g \rightarrow q\bar{q}$, $g \rightarrow gg$ are used to produce events with differing numbers of final state partons. This model allows the inclusion of higher order effects but is based on the assumption that only a few "leading logarithmic" diagrams are important at each order in perturbation theory. Coherence effects between soft gluons are included by forcing the opening angle between successive splittings to narrow as the shower develops. In JETSET particular care is taken to ensure that the parton shower approach gives an adequate description of the properties of three jet events as predicted by second order matrix elements.

Stage (iii) involves the hadronization of the coloured partons produced in the parton shower. This cannot be calculated using perturbation theory and, in the case of JETSET, is simulated using the LUND string model [20]. In this model, which exhibits Lorentz covariance and is based loosely on QCD, the hadronization process is pictured

as the break up of a massless relativistic string. This string corresponds to the colour flux tube stretched between two coloured objects. At each string break a light $q\bar{q}$ pair is generated with the relative probabilities of producing $u\bar{u} : d\bar{d} : s\bar{s}$ pairs being 1:1:0.3. The initial quark is combined with the antiquark produced in the string break to form a colour singlet meson. This process is repeated with the remaining $q\bar{q}$ system until there is no longer enough energy to allow further $q\bar{q}$ pair production. Baryon production is incorporated by allowing, with the relevant probability, the production of a diquark-antidiquark pair at the string break. The relative baryonic production rate was tuned to reproduce data taken at lower energies.

At each string break the fraction of the available quark energy taken by the hadron is parameterized, for light quarks, using the LUND symmetric fragmentation function,

$$f(z) \propto \frac{(1-z)^a}{z} \exp(\frac{-bm_\perp^2}{z}) \quad \text{with} \quad z = \frac{(E+p_{||})_{\text{hadron}}}{(E+p)_{\text{quark}}}$$

where $(E+p)_{\text{quark}}$ is the quark energy and momentum after the parton shower, $(E+p_{||})_{\text{hadron}}$ is the hadron energy and momentum component parallel to the quark direction, $m_\perp$ is the transverse mass of the produced meson, and a and b are parameters to be determined experimentally. For heavy quarks (b, c) it has been shown experimentally [21] that the LUND symmetric fragmentation function predicts a spectrum which is too soft. The data seem to be better described by the Peterson [22] fragmentation function,

$$f(z) \propto \frac{1}{z[1-\frac{1}{z}-\frac{\epsilon_q}{(1-z)}]^2}$$

where ϵ_q is a parameter to be determined experimentally for each heavy quark flavour.

Some of the hadrons produced in the fragmentation process have very short lifetimes and those which are certain to decay before reaching the detector are decayed by JETSET. The kinematics of the majority of these decays are determined purely from phase space considerations. Where necessary, matrix element modifications have been made, for example, to treat properly the Dalitz decays of a π^0. Various models for beauty hadron decay have been implemented, with that of Kröner-Schuler [23] being used by default. Where possible the branching ratios used are taken from experimental measurements; however some are nothing more than reasonable guesses. Much effort

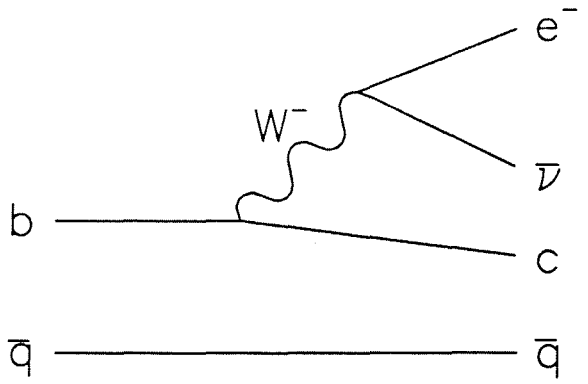

Figure 1.5: *Semileptonic decay of a beauty hadron.*

has gone into ensuring that the heavy flavour branching ratios used are up to date [24].

1.5 Semileptonic Decays of Heavy Flavour Hadrons

The heavy flavour hadrons produced in Z decays are unstable and decay with lifetimes of order one picosecond. Their decays result in the production of one or more lower mass hadrons which, in the case of semileptonic decays, are accompanied by a lepton-antineutrino pair. In the *spectator model* the decay of the heavy flavour hadron is approximated by the decay of a *free* heavy quark. The validity of this model is believed to increase with the mass of the decaying heavy flavour quark. This is because QCD loop corrections, involving heavy quark propagators (in loop diagrams), become less important as the mass of that propagator increases. The Feynman diagram relevant to the spectator model decay of a beauty meson is shown in figure 1.5.

Within the framework of the spectator model all beauty hadrons are predicted to have identical lifetimes and semileptonic branching ratios. The momentum spectrum of the lepton produced in the decay of beauty hadrons is the same shape as that of the electron produced in muon decay. In the case of charm hadron decays the spectrum would be slightly softer, similar in shape to that of the antineutrino produced in muon decay. The endpoint of the lepton momentum spectrum is principally determined by the mass of the decaying hadron, and is therefore significantly larger for beauty decays.

For this analysis the semileptonic decays of the beauty hadrons were simulated using

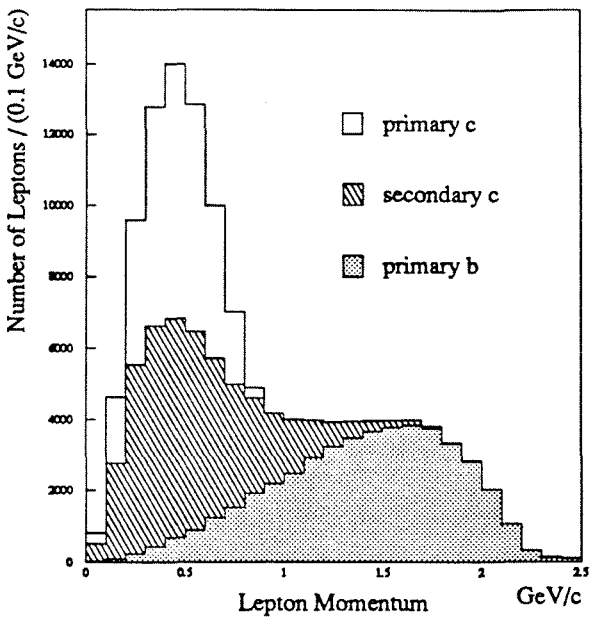

Figure 1.6: *Spectator model predictions for the momentum spectra of leptons produced in heavy flavour decays.*

the Kröner-Schuler model [23]. This model uses QCD based calculations to take into account the helicity structure of the decaying W. These corrections are important as the lepton spectra associated with the different W helicities are markedly different. The model was tuned to reproduce accurately the shape of the lepton momentum distribution observed in $\Upsilon(4S)$ decays [25]. The CKM suppressed decay $b \rightarrow u$ was simulated with the 1% branching fraction measured by experiments at the $\Upsilon(4S)$ [26].

Spectator model predictions for the "rest frame" momentum of leptons produced in heavy flavour decays are shown in figure 1.6 for a sample of simulated hadronic Z decays. In the case of primary beauty and secondary charm decays the rest frame is that of the decaying beauty hadron, whilst in primary charm decays the rest frame is that of the decaying charm hadron. It is clear that a high purity sample of primary beauty decays could, in principle, be obtained by selecting leptons with a rest frame momentum of greater than 1 GeV/c.

The semileptonic branching ratio of beauty hadrons has been measured in e^+e^- annihilation events both on resonance, at the $\Upsilon(4S)$ [25], and in the continuum, at centre of mass energies around 30 GeV/c [21]. In principle the most accurate measurement

should come from the $\Upsilon(4S)$ where the beauty hadrons are produced essentially at rest and so fragmentation effects are not a problem. However, for kinematic reasons, the mixture of beauty hadrons produced in $\Upsilon(4S)$ decays may be different from that produced at LEP energies. The semileptonic branching ratio measured at the $\Upsilon(4S)$ may not be appropriate at LEP energies if the spectator model does not hold. Any difference should, however, be small as the production of beauty hadrons at LEP energies should be dominated by the lowest mass mesons, which are precisely those produced in $\Upsilon(4S)$ decays.

1.6 Beauty Tagging at LEP

The beauty hadrons produced at LEP energies have sizable momenta and thus do not decay at rest, unlike those produced at the $\Upsilon(4S)$. At LEP the high average momentum of their decay leptons manifests itself as a high average momentum transverse to the direction of the decaying hadron. In order to tag these beauty decays it is important to reconstruct accurately the direction of the beauty hadron from the observable final state particles.

At the lower centre of mass energies of the PEP/PETRA machines the transverse momentum was usually measured with respect to the thrust axis of an event [27]. At the higher LEP energies, however, the effects of hard gluon radiation become more apparent. This leads to an increase in the number of events with more than two observable jets. Only two of these jets will be associated with the fragmentation of beauty quarks and the subsequent decay of beauty hadrons. In such cases a better determination of the direction of the decaying hadron can be obtained by defining it using only those particles produced in the fragmentation of the beauty quark.

To achieve this, jet clustering algorithms may be used to group together hadrons associated with the fragmentation of a single parton. Semileptonic beauty decay may then be tagged by identifying leptons and selecting those having a large transverse momentum with respect to their associated jet axis. The hard fragmentation of beauty quarks leads to a higher average momentum for leptons from beauty decays than for those from other sources. Thus a modest amount of additional beauty separation may

subsequently be achieved by a cut on the lepton momentum.

Chapter 2

The ALEPH Detector

2.1 The LEP Storage Ring

The LEP (Large Electron-Positron) [28] project was conceived in 1976 as a storage ring facility to allow high precision experimental tests of the Standard Model. The ring itself is housed in a circular tunnel, 26.7 km in circumference and up to 150 m underground, at the European Laboratory for Particle Physics (CERN) near Geneva. With minor additions and modifications to the existing CERN accelerator complex it was possible to inject 4 bunches of electrons and 4 bunches of positrons into LEP at 20 GeV. These counter-rotating bunches may subsequently be accelerated to any energy below the current maximum of around 50 GeV per beam. Once the required energy has been reached the beams are stored for periods of up to 20 hours, providing collisions at up to 8 interaction regions with a frequency of 44 kHz. Operating at a centre of mass energy of 91.2 GeV and a design luminosity of 1.7×10^{31} $cm^{-2}s^{-1}$ LEP should be capable of providing 10^6 Z decays per intersection point per year. At four of these intersection points vast underground caverns have been excavated to house large particle detectors capable of recording in detail the properties of these decays. It is in one of these caverns that the ALEPH detector [29] is situated.

LEP has now been operational for more than a year and has produced half a million Z decays and achieved a peak luminosity of 7×10^{30} $cm^{-2}s^{-1}$. There are already various schemes under development to enhance and extend the performance of the LEP

machine. Increasing the luminosity by an order of magnitude, using a Pretzel scheme [30], would allow rare decay modes to be probed, searching for physics beyond the Standard Model. Polarizing the LEP beams would allow a more precise determination of $\sin^2\theta_W$ through a measurement of the left-right asymmetry. Increasing the energy above the W^+W^- threshold would allow the theoretically interesting $Z \rightarrow W^+W^-$ vertex to be investigated.

2.2 Particle Detection

In e^+e^- annihilations at LEP centre of mass energies there are many particles produced in each event. Each of these particles is of a specific type and has a definite set of dynamical variables and quantum numbers associated with it. Examples of dynamical variables are a particle's energy and momentum 4-vector, whereas quantum numbers are, for instance, its charge and spin. Particle physics detectors are designed to distinguish individual particles within a complex event structure and to associate with each one as much relevant information as possible. Among the most important quantities to measure for each particle are its

- momentum vector,
- energy,
- particle type,
- charge,
- production position,
- production cross-section.

A brief introduction to the techniques employed to measure these quantities, using modern particle physics detectors, is given in the following three sections.

2.2.1 Tracking

Charged particles passing through matter will interact electromagnetically giving rise to ionization electrons. In a gas volume it is possible to guide these free electrons, using electric and magnetic fields, onto anode sense wires maintained at a high positive potential. In the high field region around these wires a free electron will start to accelerate gaining enough energy to start ionizing the atoms around itself. An electron avalanche develops inducing a large pulse on the sense wire. If the region around the anode sense wires is instrumented with cathode pads the avalanche will also induce a signal on them through capacitive coupling. The pulse height profile on neighbouring pads can be used to determine accurately the position of the centre of the avalanche in two dimensions. The arrival time of the electron on either the pads or wires and a knowledge of the electric and magnetic fields in the drift region can be used to give information about the third dimension. A three dimensional coordinate for the production point of the ionization electron can then be calculated.

Many such ionization electrons may be produced per charged particle. Thus it may be possible to infer the trajectory (track) of a particle through the detector even though it is only possible to measure its precise position at selected points along that trajectory. If a charged particle is moving in a solenoidal magnetic field its track will form part of a helix. From the helix parameters it is possible to infer the initial momentum vector, charge and possibly even production vertex of the particle.

2.2.2 Calorimetry

As their name suggests, calorimeters are used to measure a particle's energy. They work by allowing particles to interact, both electromagnetically and strongly, in layers of high density material and then measuring the number and distribution of charged particles produced in the interaction. The particles produced may themselves interact and in this way a shower develops. The shower development stops when the particles produced in an interaction no longer have enough energy to interact again. Three dimensional segmentation of a calorimeter allows the transverse and longitudinal development of the shower to be measured. These shower profiles can be used as an aid in the identification

of incident electrons and photons. The energy resolution ΔE is principally dependent on the number of charged secondary particles produced, and as such varies as,

$$\Delta E = \frac{k}{\sqrt{E}}$$

The constant k depends on the physics of the induced interaction and also on the sampling frequency of the calorimeter. Calorimeters play an essential role in detecting neutral particles which have no tracking information.

2.2.3 Luminosity Measurement

For the majority of physics studies it is necessary not only to observe a given process but also to measure the probability with which it occurs, its cross-section. In e^+e^- collisions this is usually accomplished by measuring the rate for small angle Bhabha ($e^+e^- \rightarrow \gamma \rightarrow e^+e^-$) scattering. The rate for this process is governed purely by QED and can be calculated theoretically with very high accuracy. From the ratio of observed events to Bhabhas an absolute cross-section for any physics process may be obtained.

2.3 ALEPH

2.3.1 The ALEPH Detector

The ALEPH detector [29] was designed as a high precision instrument to probe physics processes in the 80 to 200 GeV centre of mass energy region. It had to be capable of processing events at a rate of 1 Hz around the Z peak, while remaining flexible enough to be able to observe any possible signatures of new physics in the continuum below 200 GeV. This led to the design of a general purpose detector, covering as much of the solid angle around the interaction point as practical, with emphasis on high precision three dimensional tracking and highly granular calorimetry. Particle identification is attempted by a rate of energy loss technique as well as by the calorimeters.

It is not practical to measure all the properties of an event using a single detector and ALEPH is therefore composed of 9 subdetectors, as shown in figure 2.1. Each of these subdetectors measures specific properties of the particles produced in an event.

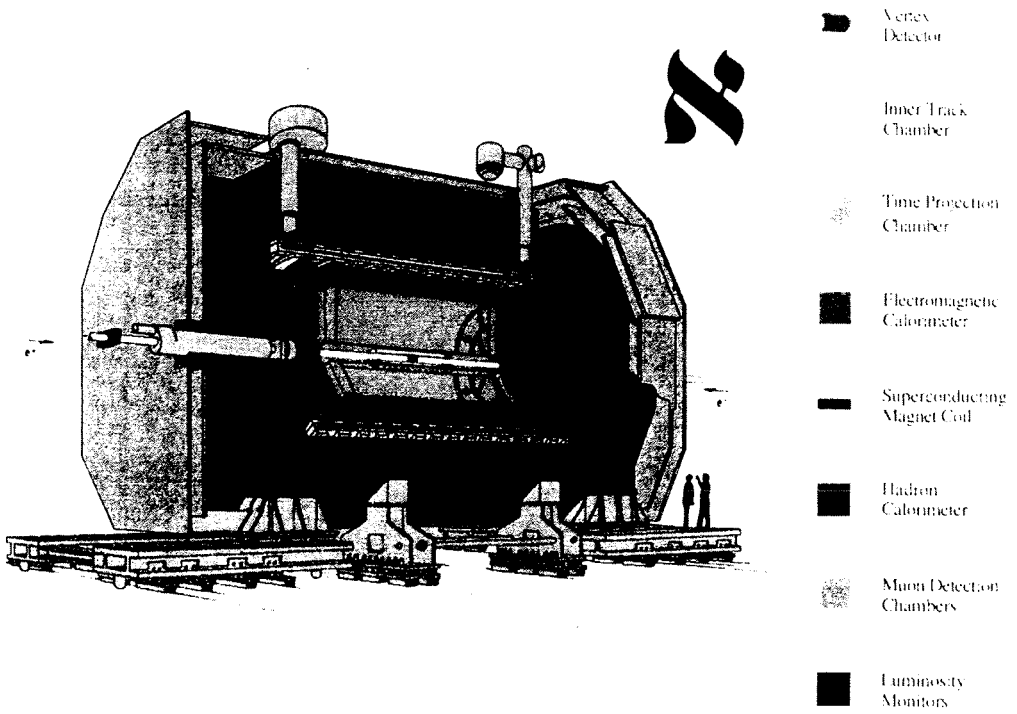

Figure 2.1: *Cutaway diagram of the ALEPH detector showing its component subdetectors.*

Only when the information from each constituent subdetector is brought together can a detailed picture of the whole event be drawn.

After a brief review of the ALEPH coordinate system a short description of each of these subdetectors will be given, indicating their role within ALEPH. These different detectors are classified, according to the type of information they provide, into the following categories,

- tracking detectors,
- calorimeters,
- luminosity monitors.

2.3.2 The ALEPH Coordinate System

The coordinate system used to describe the ALEPH detector is the one which is conventionally adopted in e^+e^- experiments. Its origin is the theoretical beam crossing

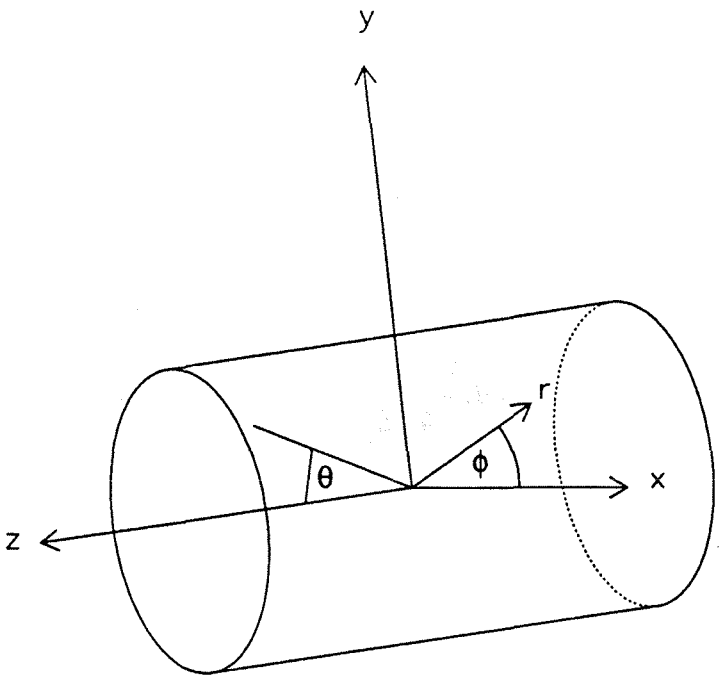

Figure 2.2: *The coordinate systems used to describe the ALEPH detector.*

point. The positive z axis is defined to be along the nominal direction of the emerging e^- beam. The positive x axis points towards the centre of the LEP ring. The y axis is orthogonal to both of these, with positive y pointing vertically upwards.

It is also useful to define another coordinate system (r, θ, ϕ) such that

$$x = r\cos\phi,\ y = r\sin\phi,\ z = r\cot\theta$$

These two coordinate systems are shown in figure 2.2.

2.4 The Tracking Detectors

2.4.1 The Time Projection Chamber

ALEPH's main tracking chamber is a large second generation Time Projection Chamber (TPC). It operates in the 1.5 Tesla solenoidal magnetic field produced by the superconducting coil and measures both the position and momentum of charged particles traversing its active volume, 4.4 m in length and between 0.38 m and 1.7 m in radius. The active volume is an $Ar{:}CH_4$(91%:9%) gas mixture maintained at atmospheric pressure. The TPC has a cylindrical structure with two instrumented endplates and

a central membrane maintained at around -25 kV to provide a uniform electric drift field. Each endplate is equipped with 18 multi-wire proportional chambers (sectors). The wires within a sector are strung perpendicular to the radial direction with a 4 mm spacing. Behind these anode wire planes there are rows of cathode readout pads measuring 30 mm along the radial direction and 6.7 mm perpendicular to it. This particular configuration of wires and pads was chosen to give optimal momentum resolution for high momentum tracks originating from the interaction point. The ionization electrons produced in the gas volume drift along the electric field lines towards the endplates, as shown in figure 2.3. They are constrained to drift in very tight spirals by the very strong magnetic field. These electrons cause avalanches which in turn induce signals on both the anode wires and cathode pads. In general the passage of a single particle will induce pulses on two or more neighbouring pads (a cluster). A local r-ϕ coordinate is calculated from a cluster by weighting with the relative pulse height distributions. The arrival time of the ionization electron at the wire plane is obtained by sampling the pulse height on the pads as a function of time. The formation of a three dimensional global coordinate from these two measurements requires a knowledge of the electron drift velocity as well as accurate maps of the electric and magnetic fields in the drift region. These were obtained with the aid of a laser calibration system, capable of producing 30 straight *tracks* at different angles through the drift volume. The r-ϕ spatial resolution depends on several factors including the uniformity of the electric and magnetic fields and the angle of the track with respect to the wires and the pads. The average r-ϕ spatial resolution obtained is of order 170 μm. The average z spatial resolution obtained is of order 1 mm and is optimal for tracks with θ angles around 90°.

The TPC has 21 concentric pad rows and can therefore measure up to 21 accurate space points over 80% of the solid angle. Over 96% of the solid angle more than 4 space points may be obtained. The space points measured in the TPC may be linked together forming tracks. With 21 coordinates the projection of the momentum (p_t) onto the r-ϕ plane of these tracks can be measured with a resolution Δp_t given by

$$\frac{\Delta p_t}{p_t^2} = 1.2 \times 10^{-3}\ (\mathrm{GeV/c})^{-1}$$

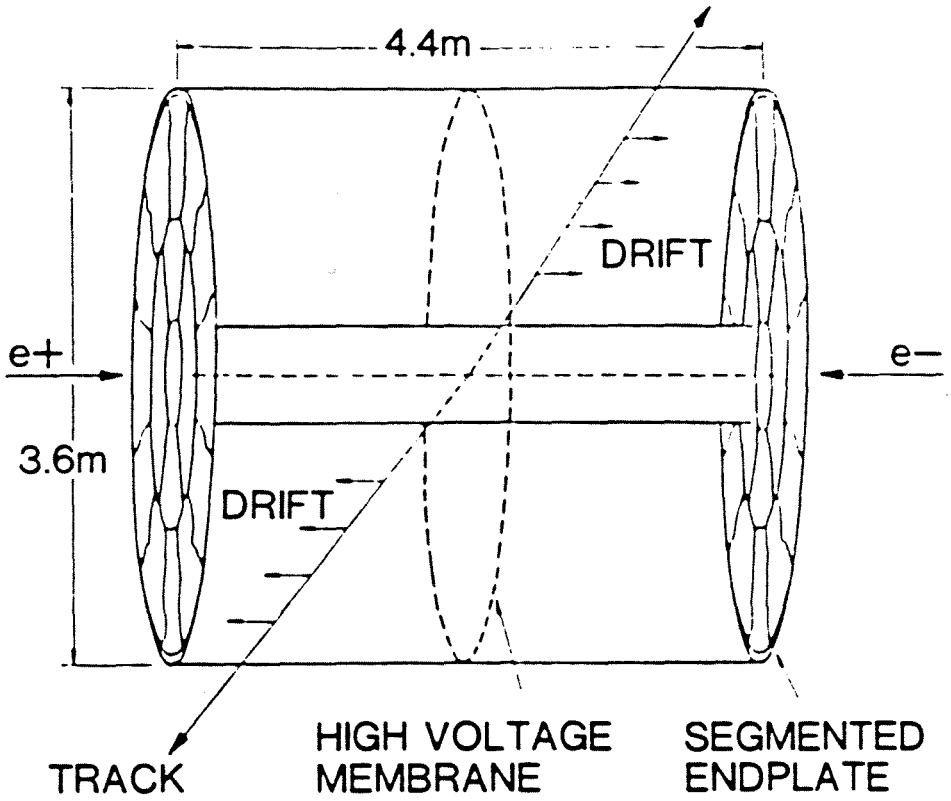

Figure 2.3: *Schematic diagram depicting the passage of two charged tracks through the TPC.*

The rate of energy loss by ionization (dE/dx) along these tracks can be measured by looking at the pulse heights induced on the sense wires crossed by the tracks. For a straight track a maximum of around 330 individual pulse height samples may be obtained. For tracks having 330 wire samples, the resolution obtained on the dE/dx measurement is around 5.2%. This dE/dx measurement can be used to provide useful particle identification (π/e separation of around 10^{-3}) in the momentum region below 5 GeV/c.

2.4.2 The Inner Tracking Chamber

The Inner Tracking Chamber (ITC) sits inside the TPC. It is a conventional drift chamber consisting of 8 concentric layers of wires strung parallel to the beam direction. The inner 4 layers each contain 96 drift cells while the outer four each have 144. The active area of the chamber is 2 m in length and between 12.8 and 28.8 cm radially. The ITC provides up to 8 space points per track over 96% of the solid angle surrounding the interaction point. Operating at 1.9 kV with an Ar:CO_2(80%:20%) gas mixture at

atmospheric pressure, the resolution obtained on each of these space points was around 130 μm in r-ϕ and 7 cm in z. The z coordinate is measured using a time expansion technique.

Tracks found in the TPC are extrapolated back into the ITC and matched with coordinates found there. Before this can be done the relative alignment of the ITC and TPC must be measured and this was achieved using a sample of high momentum tracks from $Z \rightarrow \mu^+\mu^-$ events. Using the ITC coordinates improves the measurement of all the track fit parameters. Using both ITC and TPC coordinates the resolution obtained on the impact parameter was measured to be 140 μm. An impact parameter resolution of this order may be used to determine the lifetimes of the long lived beauty hadrons. As the ITC covers a larger solid angle than the TPC it can also be used to find tracks at small polar angles with respect to the beam. When the Minivertex detector is present the ITC provides important information for extrapolation between the TPC and Minivertex hits. When the Minivertex detector is not present the ITC itself provides useful vertex information.

2.4.3 The Minivertex Detector

The Minivertex Detector (MVD) is a silicon microstrip detector used to give high precision vertex information useful in reconstructing the decay vertices of short lived particles. It was not used in the following analysis.

2.5 The Calorimeters

2.5.1 The Electromagnetic Calorimeter

The Electromagnetic Calorimeter (ECAL) consists of three sections, a barrel and two endcaps, each of which are made up from 12 modules. It is outside the TPC but inside the superconducting coil and therefore operates in the magnetic field. It is a sampling calorimeter based on 45 alternating layers of lead and wire chamber planes. The composition of one of these layer is shown in figure 2.4. Incoming particles may interact in the lead causing showers to develop. The charged particles (mostly elec-

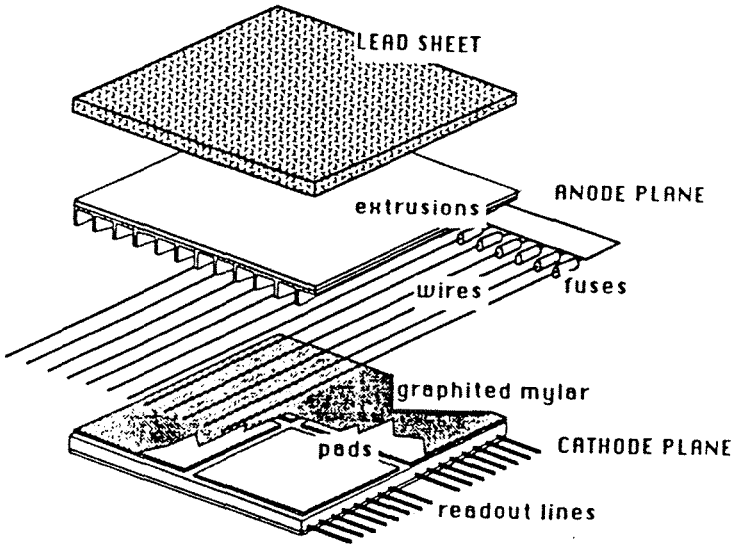

Figure 2.4: *The composition of a single ECAL layer*

trons) in these showers induce avalanches on the wire planes, which are operating in a $Xe{:}CO_2(80\%{:}20\%)$ gas mixture. These avalanches induce signals on cathode pads which are 3×3 cm^2 in size and etched onto mylar sheet. The cathode pads from all 45 layers are arranged in a projecting tower geometry, with each tower pointing back towards the interaction point. There are 70,000 such towers giving the ECAL an average granularity of 11×11 mrad^2. The 45 pads in each tower are grouped into 3 *storeys* having 10, 23 and 12 layers respectively; constituting in turn 4, 9 and 9 radiation lengths. All the pads within a storey are connected together and only one pulse height is measured per storey. The pulse heights from neighbouring storeys are clustered together to give a measurement of the energy (E) of the incident particle. For electromagnetic showers the energy resolution (ΔE) is measured to be

$$\Delta E = \frac{18\%}{\sqrt{E}}$$

The pulse height distribution within neighbouring storeys can be used, in conjunction with the momentum measurement provided by the TPC and ITC, to identify electrons and photons among the incident particles. Using this information a π/e rejection

of 10^{-3} can be obtained at energies above 5 GeV.

2.5.2 The Hadron Calorimeter

It is likely that strongly interacting particles, and muons, will emerge from the ECAL without depositing all their energy. These particles may subsequently be detected in the Hadron Calorimeter (HCAL). The HCAL surrounds the superconducting coil, for which it acts as the return yoke. It is rotated by 2° with respect to the ECAL to avoid overlapping cracks in both calorimeters. The HCAL is similar in general structure to the ECAL. It has 23 layers each composed of a thick iron slab followed by a layer of 1×1 cm^2 steamer tubes and then an array of 30×30 cm^2 cathode pads. The first 22 iron slabs are 5 cm thick and the final one is 10 cm thick, giving a total of 7.2 interaction lengths at normal incidence. Incident hadrons may interact strongly in the iron producing secondary particles which can be detected in the streamer tubes via their electromagnetic interaction. The streamer tubes are operated in limited streamer mode, at 4.25 kV with an Ar:CO_2:C_4H_{10}(13%:57%:30%) gas mixture. In this mode of operation one, and only one, avalanche should be produced each time a charged particle traverses a streamer tube. The pads are connected together in a projecting geometry. The pulse height measured on the pads is proportional to the number of streamers generated and hence to the incident hadronic energy. A digital signal from the HCAL tubes is also read out on strips running parallel to each tube. The pattern of digital signals observed on successive layers may be used as an aid in muon identification.

A section of an HCAL barrel module, showing the arrangement of consecutive layers of iron slabs, streamer tubes and cathode pads, is shown in figure 2.5.

2.5.3 The Muon Chambers

Particles exiting the HCAL have a high probability of being muons but could also be pions or kaons which have not interacted strongly in the HCAL or have interacted very late. The muon chambers have 2 layers and provide two coordinates per layer per hit. The pattern of hits observed in these chambers can be used to identify late reacting hadrons and the two dimensional information should enable improved matching of

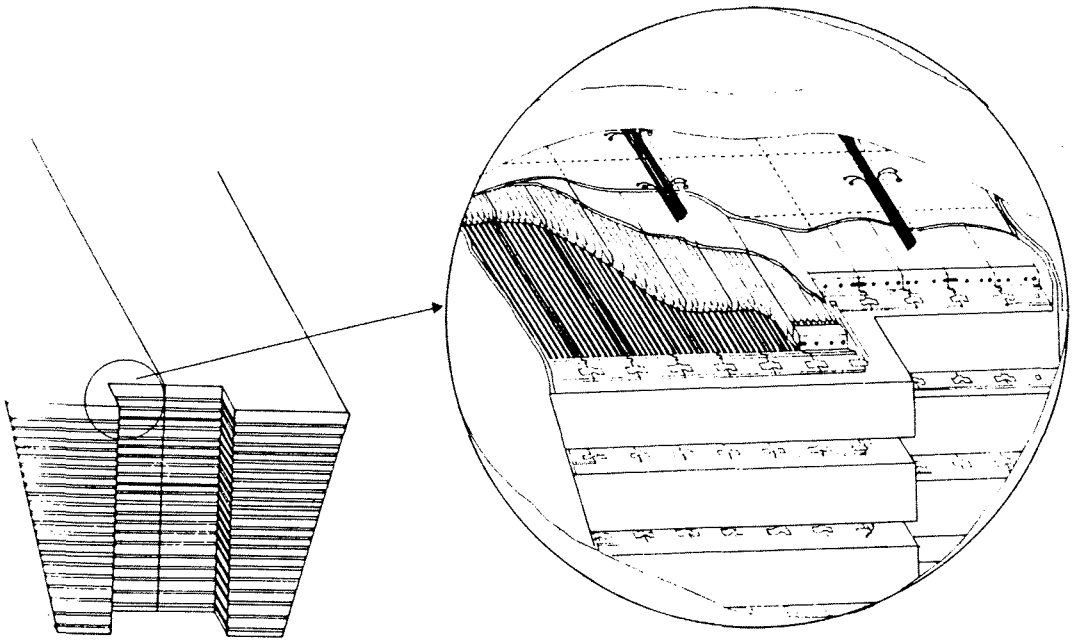

Figure 2.5: *A section of an HCAL barrel module, showing the arrangement of consecutive layers of iron slabs, streamer tubes and cathode pads.*

digital hits to TPC tracks. These chambers did not operate at full efficiency during 1989, and were not used in the following analysis.

2.6 The Luminosity Monitors

2.6.1 The Luminosity Calorimeter

The Luminosity Calorimeter (LCAL) is almost identical in construction to the ECAL and combining them gives hermetic electromagnetic calorimetry over 99% of the solid angle. It consists of 4 semicircular sections, with an inner radius of 10 cm, surrounding the beam pipe, and situated at ± 2.7 m in z. The high granularity of the LCAL is crucial in reducing the systematic error in the luminosity measurement by providing a very accurate acceptance boundary for the device. The shower profile can then be used to determine whether or not a given particle has fallen within this acceptance region. This method of luminosity measurement can be very well modelled using Monte Carlo techniques and gives an estimated systematic error of 1% on the measured luminosity.

2.6.2 The Small Angle Tracker

The Small Angle Tracker (SATR) provides accurate tracking information for Bhabha events. It is mounted onto the front of the LCAL and consists of 9 layers of drift tubes angled at 15° with respect to each other. This arrangement produces a position resolution of 200 μm. The tracking information provided by the SATR is used to define accurately the absolute location of the LCAL's sensitive region with respect to the interaction region. This further improves the systematic uncertainty in the luminosity measurement.

2.6.3 The Beam Calorimeter

The Beam Calorimeter BCAL is situated around the beampipe at ± 7 m from the interaction point. It sits behind the superconducting quadrupoles and therefore has a Bhabha rate which is 20 times higher than that of the LCAL. This monitor is used to give an online determination of the luminosity within a run and also to give an indication of background conditions.

Chapter 3

Triggering, Data Acquisition, Detector Simulation and Event Reconstruction

3.1 Triggering

3.1.1 Triggering at LEP

At each interaction point the LEP beams cross at a frequency of 44 kHz. The production rate of interesting events is much lower (below 1 Hz) even at design luminosity. With current technology it is only possible to record events for subsequent analysis at a rate of around 10 Hz. It is the job of a triggering system to select all the interesting events, while rejecting the largest possible fraction of the uninteresting background events. At LEP these background events are mainly produced by beam gas interactions and off-momentum beam particles colliding with either the beam pipe or the collimators. The trigger must be efficient to minimize the time when the detector is unable to process a new event (the dead time). It is equally important that the triggering system does not introduce undesirable biases into the event sample it selects.

3.1.2 The ALEPH Approach

The ALEPH triggering system was designed to select processes as diverse as $Z \rightarrow q\bar{q}$ and $Z \rightarrow \nu\bar{\nu}\gamma$, whilst maintaining the overall data taking rates at a manageable level by rejecting uninteresting background events. To achieve these aims it utilizes, individually and in combination, signals from different subdetector components. Each subdetector component provides 60 independent trigger signals, corresponding to a division of the solid angle into 60 θ-ϕ segments. By combining the signals from different subdetectors corresponding to a single θ-ϕ segment it is possible to trigger on both single particles and mono-jets. Alternatively summing all 60 segments from one of the calorimeters will allow triggering on the total energy of an event. To minimize the associated dead time the triggering decision was split into three levels.

- Level 1 : With signals from the ITC, ECAL, HCAL and LCAL a trigger decision is made in 5 μs with a maximum acceptance rate of 500 Hz.

- Level 2 : The ITC signals of the level 1 trigger are replaced by the corresponding TPC signals. This allows a validation of the level 1 decision within 63 μs. Events satisfying the level 2 selection criteria are read out and so the acceptance rate must be less than 10 Hz.

- Level 3 : At this stage the information from all the different subdetectors is available. Software processing is used to analyse information coming from different subdetectors. The outcome of this software processing is used to limit the data recording rate to a few Hz.

3.1.3 Triggering in the 1989 Runs

In the 1989 runs[1] the annihilation events were triggered by one or more of the following

- a total energy requirement in the ECAL alone,

- a coincidence between an ITC track and ECAL energy,

[1]More details, including the thresholds and pre-scaling factors, of the triggering configuration used during this period are given in [14].

- a coincidence between an ITC track and penetration in the HCAL.

Luminosity events were triggered by one or both of,

- a coincidence in energy deposition between geometrically opposite LCAL modules,
- energy deposition in a single LCAL module.

Most events were triggered by more than one of the above criteria and this redundancy allowed the efficiency of the trigger system to be calculated. The efficiency was measured to be almost 100% for leptonic and hadronic Z decays and 99.7 $\pm$0.2% for Bhabhas[2].

The extremely favourable background conditions provided by the LEP machine allowed the level 1 trigger rate to remain as low as 0.5 Hz for a luminosity of 10^{-30} $cm^{-2}s^{-1}$. This allowed ALEPH to take data, for most of the 1989 running period, using only the level 1 trigger. The other two levels were commissioned towards the end of the year and were subsequently used to further reduce the level of background. Of the half a million events accepted during 1989 over 85,000 were either Z decays or Bhabhas.

3.1.4 The ITC R-Φ Trigger

The ITC R-Φ trigger is an essential component of ALEPH's level 1 triggering system. It determines in under 1 μs whether the ITC has seen any evidence, in the r-ϕ plane, of a high momentum charged track originating from the interaction region. This decision must be made quickly in order to allow a gating technique to be used to prevent a build up of space charge in the active volume of the TPC.

The trigger takes as input the latched signals from the 960 sense wires of the ITC. It logically groups these inputs into 288 trigger masks having 12 wires each. A mask consists of a single wire in each of 4 layers and two adjacent wires in each of the other 4, see figure 3.1. The two adjacent wires from any one layer are logically ORed together. The 12 bit masks are therefore reduced to 8 bit masks, with each bit representing a layer of the chamber. Constraints are then applied to determine which 8 bit patterns

[2]These efficiencies are quoted for the relevant regions of the solid angle.

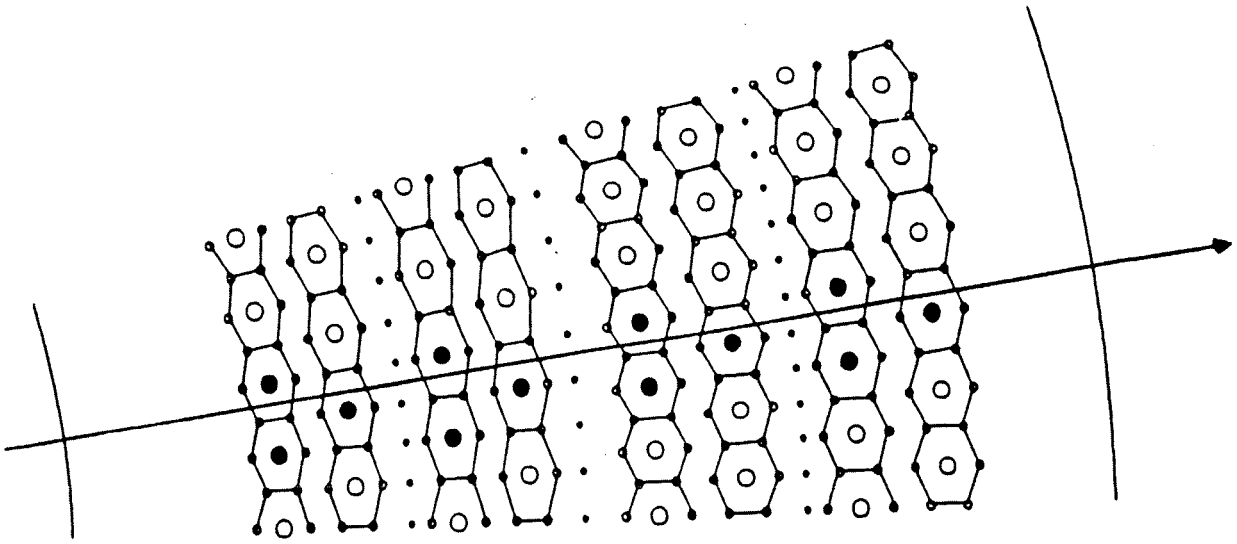

Figure 3.1: *A high momentum track is shown passing through a section of the ITC. The drift cells belonging to the relevant 12 bit trigger mask are highlighted.*

can represent a valid track, *e.g.* a track may be flagged if at least 5 out of the 8 layers have fired. In hardware terms the 12 latched wire hits corresponding to a given mask are connected to the address lines of a 12 bit look-up ram[3]. The 12 bit rams are always programmed in order to give a triggering decision in terms of a hit pattern corresponding to the eight layers of the chamber. The 288 output bits from these rams are ORed in neighbouring groups to determine if a track was found in one or more of 12 ϕ sectors. The mapping of trigger signals in these 12 ϕ sectors onto the 60 ALEPH θ-ϕ sectors is software selectable. At present an ITC ϕ sector is mapped onto a calorimeter θ-ϕ sector if a particle originating from the interaction point, with a transverse momentum of over 1 GeV/c, could possibly have caused trigger signals in both of them.

As well as the basic track trigger outlined above, the R-Φ trigger hardware also provides a variety of special signals which may be used to define more complex triggers. These include triggers or vetoes based on both the total number of tracks (or groups of neighbouring tracks) found in the event and the total number of hits (or groups of

[3]In actual fact the 12 bit conceptual rams are implemented in 14 bit rams but this should be transparent to any user.

neighbouring hits) found in each layer of the chamber. There is also a back-to-back trigger bit which is set if two tracks exit the chamber at geometrically opposite ϕ angles.

The R-Φ trigger processor consists of 9 wire-wrapped FASTBUS slave modules, 8 identical integral boards and one processor board. The boards were designed and produced by an engineer working at the Rutherford Appleton Laboratory. I was heavily involved with him in testing these boards, from debugging the initial prototype through to commissioning the final working system. This involved ensuring that the boards conformed to the FASTBUS standard as well as resolving design misunderstandings and diagnosing hardware faults. The system design allows 960 fake wire hits, simulating real data, to be written to the inputs of the integral boards. Enough information can be read out from the boards to allow each individual stage of the trigger decision to be checked. This proved to be an invaluable aid in localizing and diagnosing hardware faults. As far as possible each board was tested in isolation until all the faults were fixed. A large software package was written which, when given as input the 960 wire latches, would predict at each intermediate stage the responses of the hardware modules. By generating random patterns of wire latch inputs and loading them into the trigger it was possible to compare the hardware's response with that of the software simulation. Repeating this process with many random inputs eventually allowed all the hardware faults to be ironed out.

It was necessary to provide a user interface to the processor to allow easy operation by a non-expert. This involved writing software which would take a physically interesting trigger requirement, like requiring 5 out of 8 layers to fire, and then loading the required bit patterns into the 14 bit rams on the integral boards. This software had to be extremely flexible as it was not, *a priori*, clear what the background conditions would be at LEP. It also had to be capable of treating dead wires, so that the trigger did not become asymmetric in its selection of interesting physics events.

The ITC R-Φ trigger was commissioned after the LEP pilot run in August 1989. Since then it has been used extensively and has performed extremely well. Each triggering decision it has made was validated online and no evidence has been found of

any resulting inefficiency[4] or bias. The basic track trigger has been used in coincidence with HCAL penetration to check the efficiency of the primary hadronic event triggers. This combination of trigger signals also provided ALEPH's only dimuon trigger. The efficiency of the dimuon trigger has been found to be almost 100%[5].

The ITC special triggers were not used in earnest until the 1990 running period. The back-to-back trigger was commissioned in order to provide a dimuon trigger independent of the HCAL. The track VETO feature was used in coincidence with a SATR trigger to select luminosity events independently of the LCAL.

In the next few years the R-Φ trigger will be superceded by a three dimensional track trigger. This *Space Point* trigger will require valid tracks to project back towards the interaction point in z as well as in r-ϕ. This will provide a higher level of background rejection at level 1, which should prove invaluable for triggering at a high luminosity LEP.

3.2 The ALEPH Data Acquisition System

The ALEPH detector has over 700,000 electronics channels which were predicted to deliver up to 500 Megabytes of raw data per second. It is the task of the ALEPH data acquisition system to manage the collection and compression of this data ready for later reconstruction. To handle the huge data rates involved a tree-like hierarchy was implemented with each subdetector representing a different branch of the tree, as shown in figure 3.2. This scheme allowed data compression to be performed in parallel as the data moved along the branches of the tree.

As soon as a valid trigger signal was received the front-end electronics of each subdetector would begin digitizing the signals which they had received. Subdetector event builders would then read the data from the front-end and perform any reformatting and compression necessary, producing a complete subdetector event. The event builders would then append a run and event number to this subdetector event. At the next stage a main event builder would read in these subdetector events and combine them to form

[4]Except for a brief period when the chamber itself was not operating at full efficiency.

[5]The method used assumed that the two signals caused by the two muons were independent.

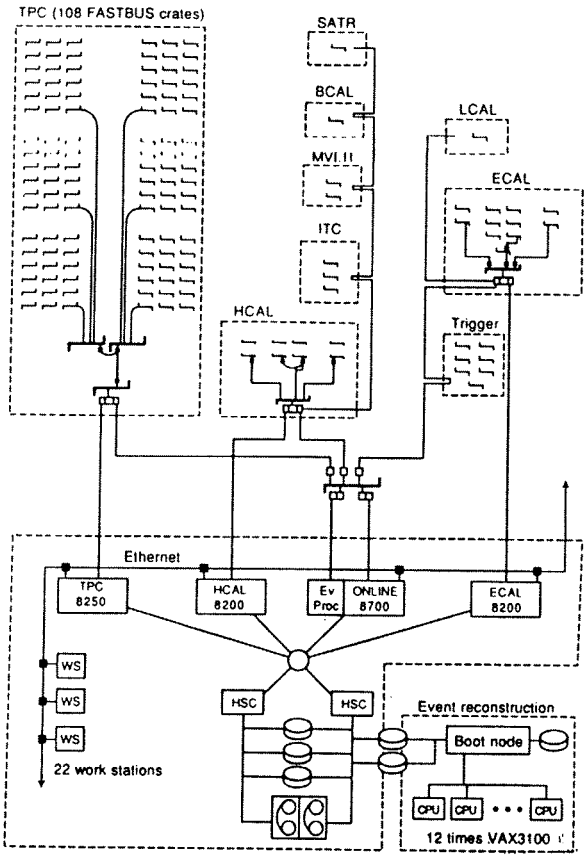

Figure 3.2: *Overview of the ALEPH data acquisition system.*

a complete event ready to be read by the main VAX computer for permanent storage.

At each stage the quality of the data was monitored and if any serious problem was found the data acquisition was paused and a message sent to the operator allowing him to take appropriate action. The system would not, for instance, allow the passage of an incomplete event as this would only cause a problem at the analysis stage. When the data from an event reached the VAX, many tools, including online histogramming and an event display, were used to trace problems with the detector hardware.

3.3 Detector Simulation

The ALEPH detector is so complex, and the interactions of particles with it so varied, that the raw digitizings it produces are difficult to interpret without the aid of a detector simulation package. For the ALEPH detector this simulation is provided by a large computer program which uses Monte Carlo techniques to perform difficult integrations. This program, GALEPH, takes the particles produced by an event generator and predicts the digitizings which the detector would generate in response to their passage

through it. It is used to give estimates of detector acceptances and efficiencies as well as to study the performance of the reconstruction program.

GALEPH has access to a very detailed map of all the material present within the detector volume. It uses this map to predict what interactions will occur as a particle passes through the detector. It is, for example, necessary to know what the beampipe is made of, and how thick it is, in order to reproduce properly the number of photon pair conversions which it will induce. The analysis presented in this thesis relies heavily on the quality of the simulation of both the tracking and the calorimetry. These are briefly discussed in the following two paragraphs.

The path of a charged particle through the tracking volume is divided into small track elements. When each element is formed the effects of energy loss, multiple scattering, particle decay and interaction with material are taken into account. When a track passes through an active volume enough information is stored to be able to predict the hits which this track would generate in the corresponding detector elements. Only after all the tracks have been followed through the detector volume is the hit information from individual tracks brought together and used to produce digitizings. It is at this point that the errors caused by detector resolution and the effect of overlapping tracks are taken into account.

The detailed modelling of a calorimetric shower typically involves the study of hundreds of secondary particles for each particle incident on the calorimeter. This technique requires a prohibitively large amount of computer time for it to be of use in a simulation program like GALEPH. The simulation of the interactions of particles with the calorimeters was therefore performed using parameterizations for the shape of the induced showers. These parameterizations were tuned to reproduce both test-beam results and the predictions of a full detailed shower simulation.

3.4 Event Reconstruction

3.4.1 Online Reconstruction

It is the task of the event reconstruction program (JULIA) to obtain meaningful physical quantities from the myriad of digitizings produced by the detector's electronics. It is at this stage that tracks and clusters of calorimetric energy are formed and associated with each other. Certain important checks on the quality of the data can only be performed after the event reconstruction has taken place. It is therefore important that this should be carried out as soon as possible after the data has been taken. In ALEPH this is achieved by having a dedicated network of computers connected to the online system via a group of large shared disks, as shown in figure 3.2. Using this system the output of the reconstruction program is available only a few hours after the end of a given run. This is invaluable in providing an early indication of any problems which the detector has developed.

The analysis presented in this thesis makes extensive use of charged tracks, and their reconstruction will be briefly discussed in the following section. The calorimeters are only used to provide muon and electron identification, and this will be discussed more fully in the relevant chapters. For this analysis both the data and the GALEPH simulation were passed through the same version of JULIA.

3.4.2 Track Reconstruction

The measurement of three dimensional coordinates by the TPC and ITC was briefly discussed in sections 2.4.1 and 2.4.2 respectively. Groups of coordinates consistent with having been caused by the passage of a single charged particle are linked together at the *pattern recognition* stage. Tracks are then formed by fitting helices through each of these groups of points using a "Kalman Filter" [31] technique. The optimal track fit was obtained only after the effects of TPC sector-to-sector and TPC-ITC misalignments were taken into account. The raw TPC coordinates were also corrected for the effects of inhomogeneities in the electric and magnetic fields in the drift region. Both of these effects were studied [32] using dimuon events and measurements taken using the

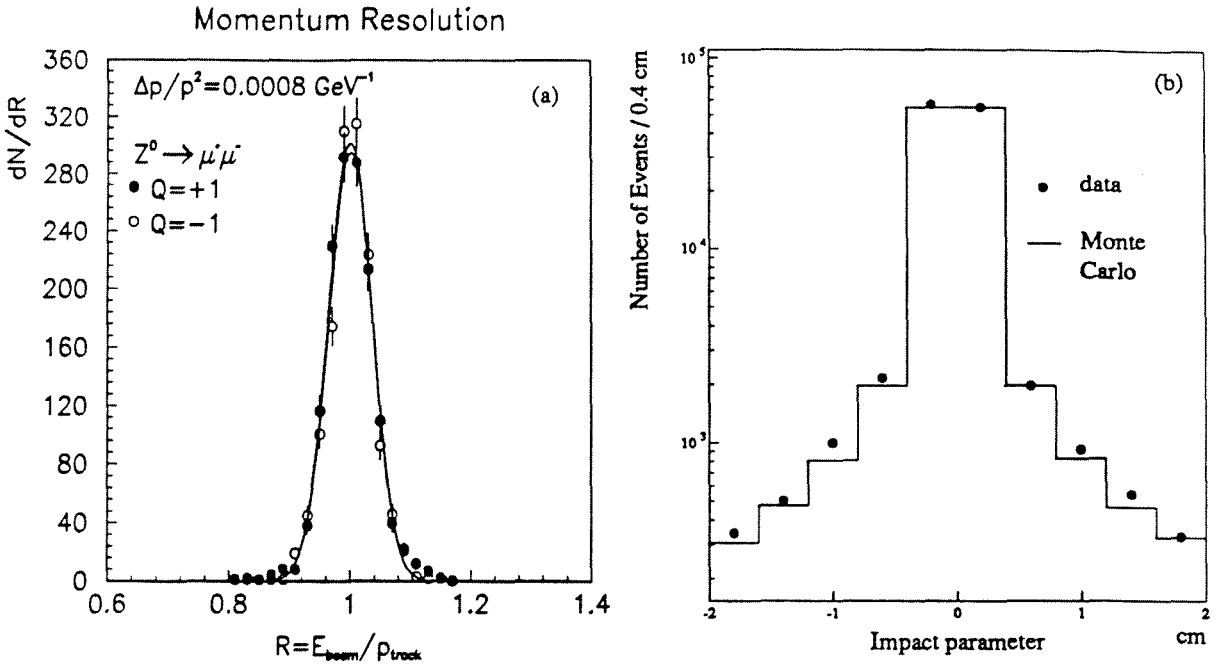

Figure 3.3: *(a) The ratio of beam energy over track momentum measured by both the TPC and the ITC for tracks in* $Z \rightarrow \mu^+\mu^-$ *events. (b) Comparison between data and Monte Carlo for the* d_0 *of tracks with* $p > 3$ GeV/c *in hadronic events.*

TPC's laser calibration system. When all the corrections were taken into account the momentum resolution obtained for dimuon events with both ITC and TPC coordinates was

$$\frac{\Delta p_t}{p_t^2} = 0.8 \times 10^{-3}\ (\mathrm{GeV/c})^{-1}$$

as shown in figure 3.3. The quality of the Monte Carlo simulation of the tracking can be seen by looking at a comparison between data and Monte Carlo, figure 3.3, for the d_0[6] of tracks with $p > 3$ GeV/c in hadronic events.

[6] d_0 is the distance of closest approach of the track to the beam axis measured in the r-ϕ plane. It is positive for tracks whose helices encircle the beam axis.

Chapter 4

Event Selection and Jet Definition

4.1 Run Selection

This analysis is based on a study of events recorded by the ALEPH detector during the 1989 LEP running period. Throughout this thesis comparisons are made between the properties of these real events and those produced by Monte Carlo simulation. The simulated events were all generated with somewhat idealized detector operating conditions. Before making comparisons between data and Monte Carlo it was necessary to ensure that, in all important respects, the data were taken when the actual operating conditions of the detector were close to the Monte Carlo ideal. For this reason runs were rejected if either

- there was any evidence of a major problem with either the ITC, TPC, ECAL or HCAL,
- or any of the hadronic event selection triggers were disabled,
- or there were fewer than 10 Bhabha events in that run.

4.2 Hadronic Event Selection

Under normal LEP operating conditions the high voltages of the tracking chambers were turned on only after the beams were stable and colliding. It was therefore important to

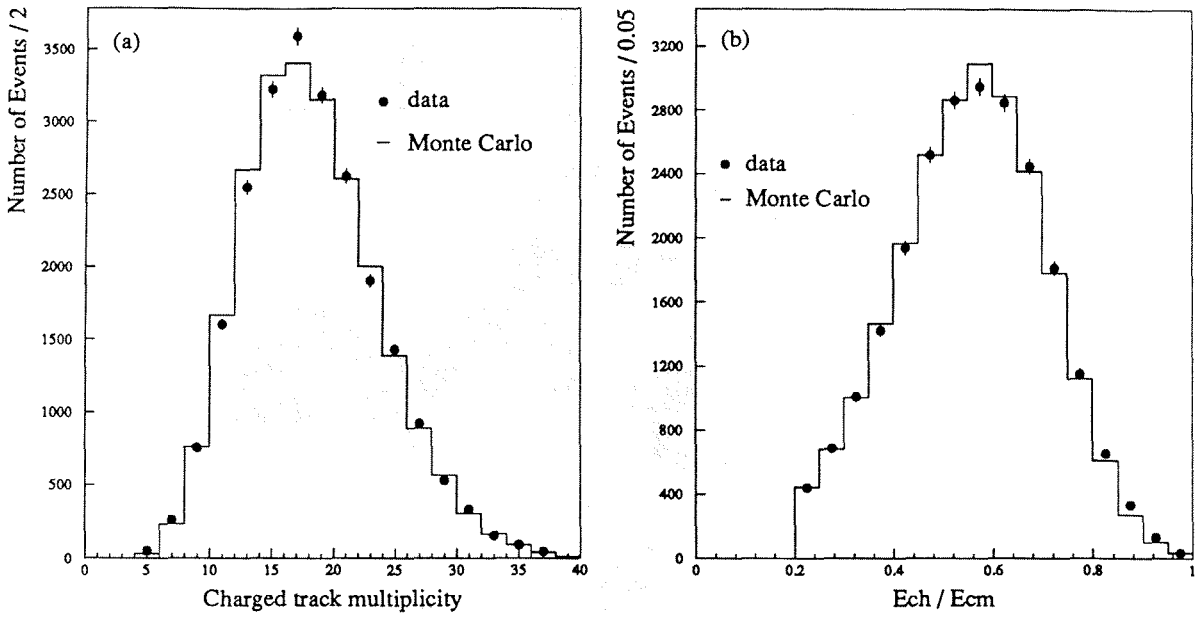

Figure 4.1: *Comparison between data and Monte Carlo for selected hadronic Z decays of (a) the charged track multiplicity and (b) the fraction of the centre of mass energy appearing as charged tracks.*

select only events where the high voltages of the ITC, TPC, ECAL and HCAL were at operational levels. For this analysis hadronic Z decays were selected using the tracking information provided by the TPC. A track was defined as *good* if it had

- at least 4 associated TPC coordinates,
- and a distance of closest approach to the interaction point of less than 10 cm along the beam line and 2 cm transverse to it,
- and $|\cos\theta| < 0.96$.

Using the tracking information an event was selected as a hadronic Z decay if it had

- at least 5 *good* tracks,
- and the sum of the charged energy (assuming pion mass) of all its *good* tracks was greater than 20% of the centre of mass energy.

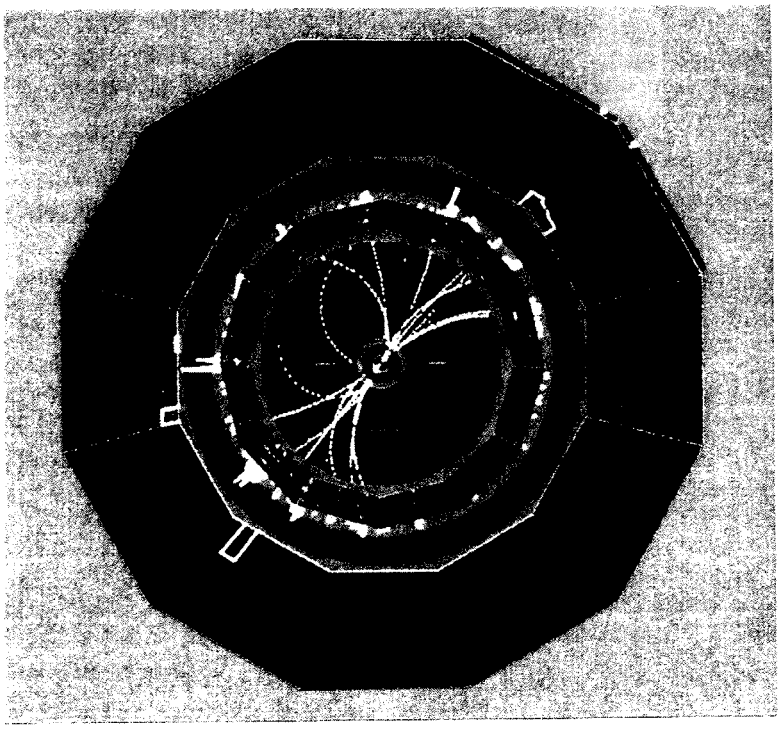

Figure 4.2: *A typical two jet event passing the hadronic event selection cuts.*

Monte Carlo simulations showed the efficiency of these selection criteria to be 94.8%, independent of quark flavour to better than 1%. They also predicted the background to this selection from $\tau^+\tau^-$and $\gamma\gamma$ events to be less than 0.3%. There was very good agreement between data and Monte Carlo for both the variables used in this event selection, see figure 4.1. A typical event passing these hadronic selection cuts is shown in figure 4.2.

4.3 Jet Finding

As outlined in Chapter 1, semileptonic decays of beauty hadrons can be tagged by identifying leptons having a large transverse momentum with respect to a jet axis. There are many different approaches to the problem of constructing a set of jet axes for a given event. Two of the most successful algorithms used for e^+e^- annihilation events are YCLUS [33] and LUCLUS [16]. These algorithms take a set of input 4-momenta, which usually correspond to the set of observed particles, and produce a set of 4-momenta corresponding to the reconstructed jets.

Initially the YCLUS algorithm defines each input 4-vector (E_i, p_i) to be a cluster. The scaled invariant mass (y_{ij}) between every possible pair of clusters i, j is then calculated as

$$y_{ij} = \frac{2E_iE_j(1-\cos\theta_{ij})}{{E_{vis}}^2}$$

where θ_{ij} is the angle between the two clusters and E_{vis} is the visible energy in the jet system. The two clusters having the smallest scaled invariant mass are combined to form one new cluster. This process is repeated with the remaining clusters until the minimum scaled invariant mass is greater than the cutoff value given by the input parameter $YCUT$. At this point the remaining clusters are called jets. The input parameter $YCUT$ acts as a jet resolution parameter, essentially determining the average jet multiplicity which will be found.

LUCLUS proceeds in a similar way but at each iteration it combines the two clusters having the smallest value of

$$\sqrt{\frac{2|p_i|^2|p_j|^2(1-\cos\theta_{ij})}{(|p_i|+|p_j|)^2}}$$

until this value exceeds the input parameter $DJOIN$ [1].

4.4 Jet Axis Definition

There is no natural definition of jet axis and the optimal choice depends on what the jets are going to be used for. For this analysis the jet axis chosen should, ideally, be the one which provides the highest purity of semileptonic beauty decays (determined from the Monte Carlo) for the required selection efficiency. Care must, however, be taken to ensure that the properties of the jets obtained using a particular definition are well described by the Monte Carlo. It would otherwise be difficult to interpret the efficiency and purity predicted by the simulation. When this analysis was carried out any attempt to include calorimetric information in the jet axis definition resulted in a

[1] To save processing time LUCLUS performs some initial clustering before combining clusters in this way but later compensates for this by allowing reassignment of particles within clusters.

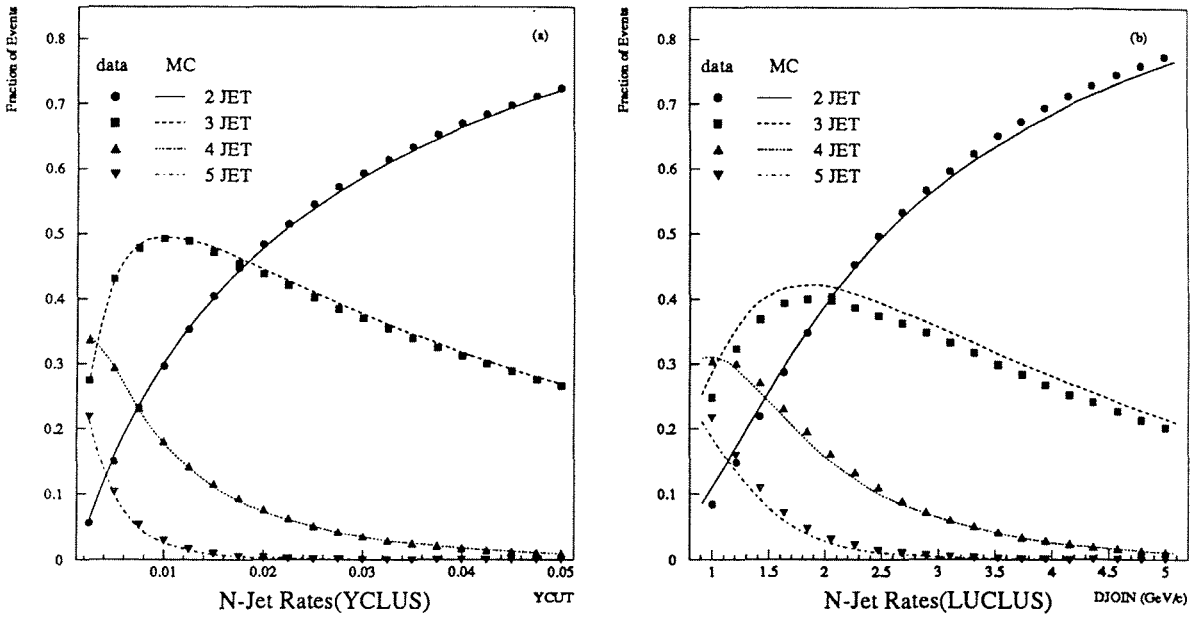

Figure 4.3: *Variation in n-jet rates with jet resolution parameter using (a) YCLUS and (b) LUCLUS.*

significant decrease in the level of agreement obtained between data and Monte Carlo. Jets were therefore defined using only the *good* charged tracks as measured by the TPC and ITC.

A good indication of how well the Monte Carlo is simulating the data, as far as jet properties are concerned, can be obtained by inspecting the variation of the n-jet rates[2] with the jet resolution parameter. The variation obtained is shown in figure 4.3, for both data and Monte Carlo, for jets formed using both YCLUS and LUCLUS. There is clearly a high level of agreement between data and Monte Carlo for the YCLUS algorithm. LUCLUS, however, seems to be more sensitive to some difference (possibly in the fragmentation process) between data and Monte Carlo. For this reason, and because the differences in efficiency and purity obtained using the two algorithms were small, YCLUS was used as the jet finding algorithm.

Comparisons were also made between data and Monte Carlo for other jet properties, such as the energy of the n^{th} most energetic jet and the number of particles in the n^{th}

[2]The n-jet rate is defined as the fraction of all events which a given clustering algorithm reconstructs as an n jet event.

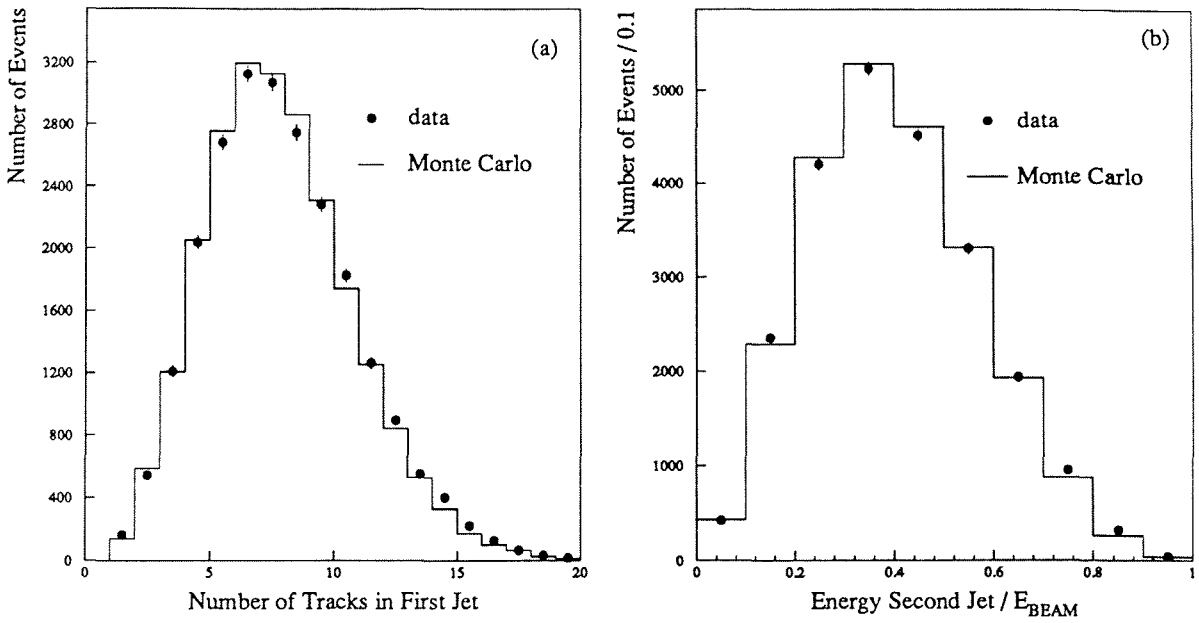

Figure 4.4: *Comparison between data and Monte Carlo for (a) the number of particles in the most energetic jet in each event and (b) the energy of the second most energetic jet in each event.*

most energetic jet. As shown in figure 4.4 these are in good agreement when the YCLUS (YCUT=0.015) algorithm is used. The level of agreement is slightly worse for the LUCLUS algorithm.

Semileptonic beauty decays can be tagged by identifying leptons having a large transverse momentum ($p_\perp$) with respect to their associated jet axis. As the jet resolution parameter is varied, the $p_\perp$ of each individual lepton may change and this can result in a reordering of leptons in $p_\perp$. To determine which value of the jet resolution parameter should be used for beauty tagging the sources of high $p_\perp$ leptons were examined in a sample of 72,000 Monte Carlo hadronic events. For each value of the jet resolution parameter, the leptons were ordered according to increasing $p_\perp$ and the top 20% selected. The source of each identified lepton in this high $p_\perp$ sample was obtained by matching the reconstructed track to the generator particle which caused it. The identified leptons were categorized as coming from either primary beauty decay, primary charm decay, secondary charm decay or from a background source. The variation in the fraction of leptons coming from each source with jet resolution parameter is

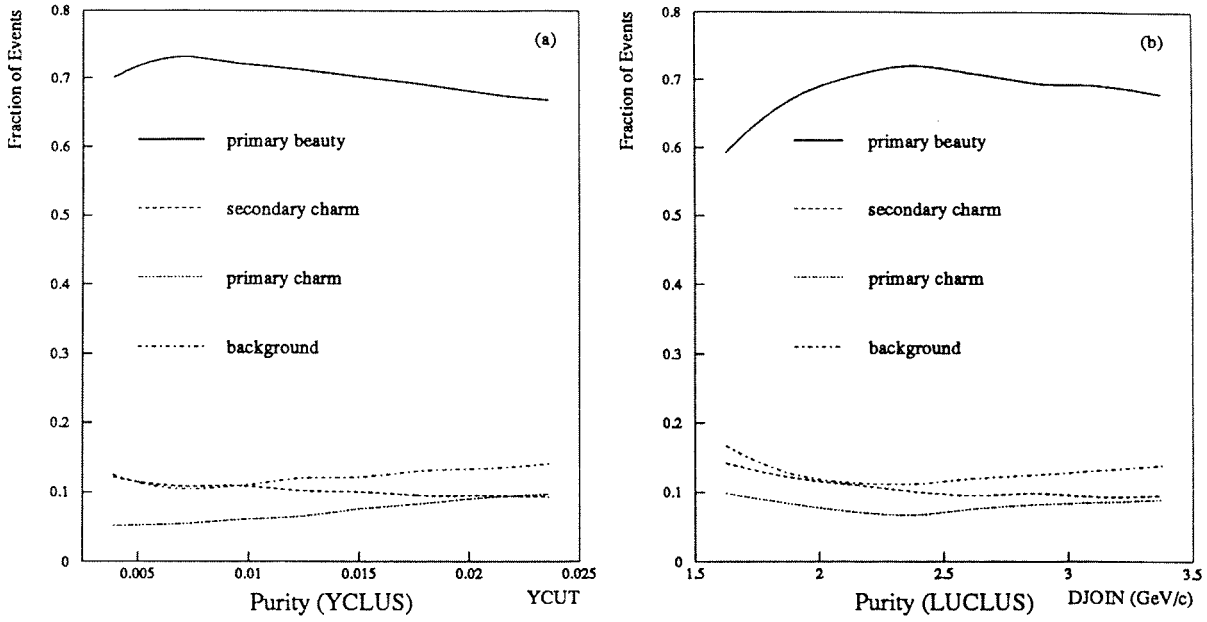

Figure 4.5: *Variation in the composition of the highest 20% of the high $p_\perp$ leptons with jet resolution parameter using (a) YCLUS and (b) LUCLUS.*

shown, for both YCLUS and LUCLUS, in figure 4.5. The purity in primary beauty decays is seen to vary by a few percent for reasonable variations in the jet resolution parameter. In the case of the YCLUS algorithm the highest purity in primary beauty decays was obtained with $YCUT = 0.007$. This value gives a ratio of 2:3:4 jet events which is substantially different from the ratio of 2:3:4 parton events predicted by second order matrix element calculations (0.40:0.55:0.05 in the case of JETSET). It is not physically obvious why the optimal purity should be obtained with such a low value of $YCUT$. Certainly the level of agreement between data and Monte Carlo for the jet properties decreases as the value of YCUT decreases. Erring on the side of caution, the actual value used in the analysis ($YCUT = 0.015$) was chosen because it gave good agreement with the parton rates predicted by second order matrix element calculations and because it gave good agreement between the jet properties observed in the data and Monte Carlo. Using the YCLUS algorithm ($YCUT = 0.015$) a further test of the ability of the Monte Carlo to describe accurately the properties of particles observed in the data was made by comparing the transverse momentum of all *good* tracks having momentum over 3 GeV/c, see figure 4.6. Also shown in this figure is a comparison

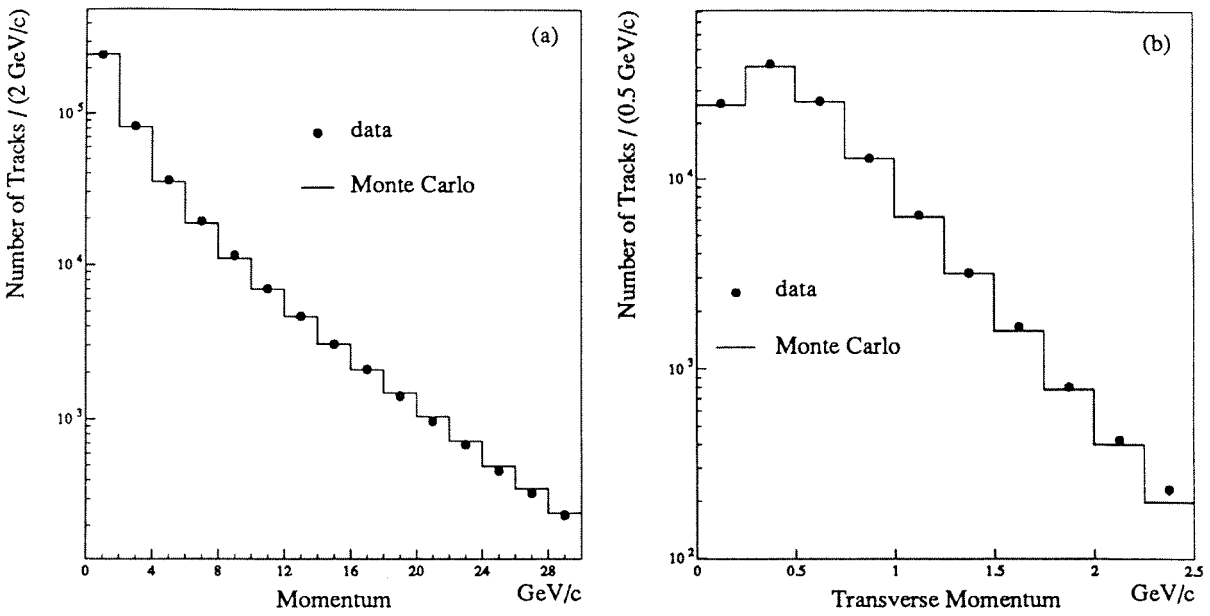

Figure 4.6: *Comparison between data and Monte Carlo for the (a) momentum and (b) transverse momentum of all good tracks with momentum above* 3 GeV/c *using YCLUS (*$YCUT = 0.015$*).*

between data and Monte Carlo for the momentum of *good* tracks.

In the published ALEPH analysis [1] an alternative definition of transverse momentum was used. In this definition ($p_{\perp(j-l)}$) the momentum of a particle is subtracted from the corresponding jet axis before its transverse momentum is calculated. This has the effect of expanding the transverse momentum scale and of slightly reordering particles within that scale.

It is, once again, not intuitively obvious which of these two definitions to adopt. The variation of the purity in primary beauty decays with jet resolution parameter was studied, as above, using the $p_{\perp(j-l)}$ definition of transverse momentum. This study showed that a modest improvement in purity, of the order of 1-2%, could indeed be achieved by adopting the $p_{\perp(j-l)}$ definition. Closer inspection showed that this increase in purity came mainly from an increased separation between heavy flavour decays and background sources rather than between the different categories of heavy flavour decays. This suggested that the increased purity obtained using the $p_{\perp(j-l)}$ definition may come from the hardness of the heavy flavour fragmentation, and not because it gave a better

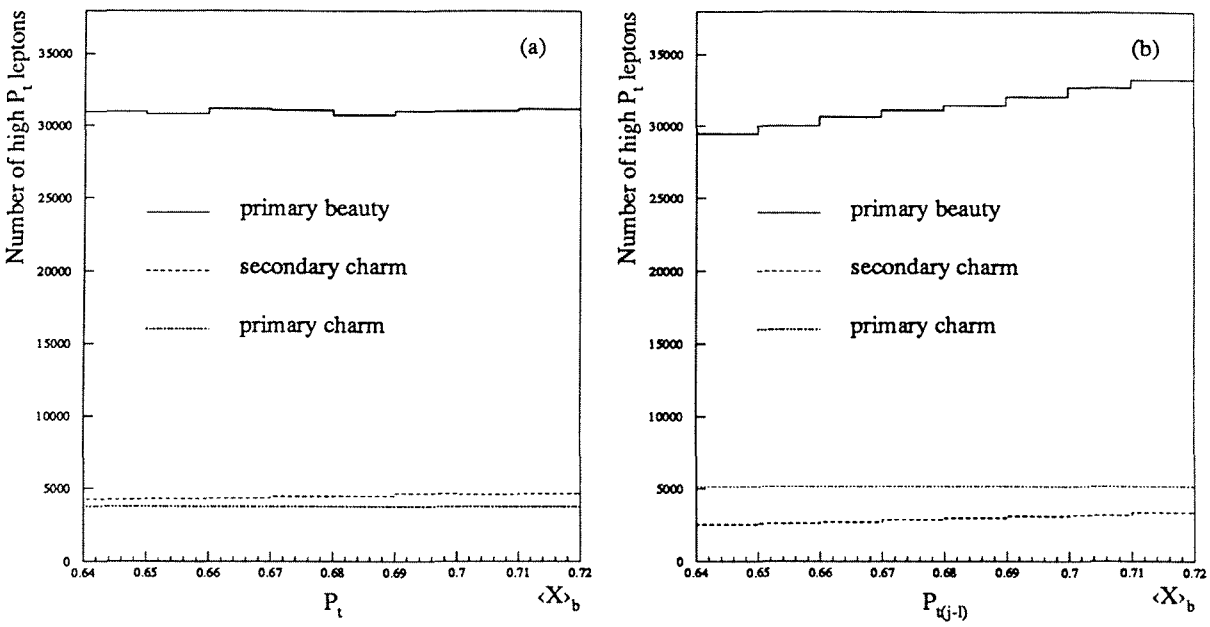

Figure 4.7: *Monte Carlo predictions for the variation of the number of leptons with high transverse momentum with the hardness of the beauty quark fragmentation ($\langle X \rangle_b$) for both the (a) $p_\perp$ and (b) $p_{\perp(j-l)}$ definitions of transverse momentum.*

definition of the direction of the heavy flavour hadron.

To investigate this hypothesis a Monte Carlo study was carried out (at the generator level) to see how the number of leptons in the high transverse momentum region varied as the hardness of the beauty quark fragmentation was changed within reasonable limits[3]. For each definition of transverse momentum the number of leptons, from different categories of heavy flavour decay, passing a given transverse momentum cut was measured as the hardness of the beauty quark fragmentation ($\langle X \rangle_b$, where $X = E_{hadron}/E_{beam}$) was increased. The transverse momentum cuts were chosen to give approximately the same efficiency for the two definitions and were $p_\perp > 1.0$ GeV/c and $p_{\perp(j-l)} > 1.75$ GeV/c respectively. The results of this study are shown in figure 4.7. For the $p_{\perp(j-l)}$ definition the number of leptons from primary beauty decay passing the transverse momentum cut increases almost linearly with $\langle X \rangle_b$. Whereas with the $p_\perp$ definition the number of leptons from primary beauty decay passing the transverse

[3]This was done by changing ϵ_b (within the limits imposed by the experimental errors quoted on $\langle X \rangle_b$ [1,34].

momentum cut is essentially independent of $\langle X \rangle_b$. Since $\langle X \rangle_b$ is only known experimentally to around 5% it is much better to use the $p_\perp$ definition. This definition also has the desirable effect of reducing the number of high $p_\perp$ leptons from primary charm decays (and hence $Z \rightarrow c\bar{c}$ events).

Chapter 5

Muon Identification

5.1 The ALEPH Approach

Muons do not interact strongly, and at the energies in question, their dominant electromagnetic interaction with matter is via ionization. They can therefore be distinguished from other charged particles by their ability to pass through many nuclear interaction lengths of material.

In ALEPH they can be identified by utilizing the tracking capabilities of the HCAL. The HCAL is an iron/streamer tube sandwich structure consisting of 23 alternating layers. A charged particle passing through a tube will usually generate a streamer which is then observed as a digital output signal. A group of adjacent digital hits in a given layer is called a cluster. Induction between tubes and the production of delta rays means that a single charged particle may fire up to four adjacent tubes in any given layer. Only clusters less than five tubes wide are likely to be solely associated with the passage of a muon. A muon is characterized by a track of such clusters penetrating through all 23 layers of iron. For this analysis identification was only performed for the barrel region of the HCAL, because only there was the digital readout of the streamer tubes fully operational for all of the 1989 data taking period.

5.2 The Identification Algorithm

The algorithm employed involves the extrapolation of all TPC tracks having a momentum over 1.8 GeV/c[1]. The tracks are extrapolated through the ECAL, superconducting coil and HCAL taking fully into account the effects of multiple scattering and the variation of the magnetic field (which is reversed in the HCAL). A cone three times larger than the rms lateral displacement due to multiple scattering is then defined around this extrapolation. Digital clusters are associated with a TPC track if they fall within its cone and are less than 5 tubes wide. At most one digital cluster was associated to a track per HCAL plane. A TPC track may be identified as a muon candidate by looking at the distribution of its associated digital clusters. A track was considered to be caused by a muon if it had

- more than 9 associated clusters in total,
- and more than 4 associated clusters in the last 10 layers,
- and more than 1 associated cluster in the last 3 layers,
- and $|\cos\theta| < 0.61$.

These cuts were optimized by studying muons in dimuon events in the data. They were chosen to be loose enough to give a high efficiency for these dimuons while being tight enough to have a low level of hadron contamination when applied to a hadronic event sample.

5.3 Calibration of the Streamer Tubes

In the data the efficiency for an individual streamer tube to give a digital hit when a particle passed through it varied within the calorimeter and also with time. Fortunately it was possible to correct for this variation by using a sample of pure muons from $Z \rightarrow \mu^+\mu^-$ events. An unbiased sample of 416 dimuon events was selected for this purpose using criteria based on tracking and ECAL information. Monte Carlo studies

[1]At normal incidence only muons having momentum over 1.8 GeV/c are likely to exit the HCAL.

estimated the purity of this sample to be greater than 99%. The digital hit information from these events was used to make an efficiency map. This map was subsequently applied to correct the Monte Carlo, which had been generated with ideal efficiency. The efficiency map gave the probability for a streamer tube to fire. The probability varied within

- 4 run periods,
- 12 modules,
- and 11 double + 1 single plane(s).

This level of granularity was chosen to correspond to a natural division of the detector in terms of high voltage supply, while still retaining a reasonable statistical accuracy on each probability obtained. The division in terms of high voltage supply was relevant because bilayers which were either drawing current or noisy were operated at a slightly reduced voltage and hence a slightly reduced efficiency. The average measured efficiency was around 70% per layer. Half of the inefficiency was caused by purely geometrical effects.

The map obtained was applied to the Monte Carlo by simply discarding a generated digital cluster with the relevant probability. Using this map, reasonably good agreement was obtained between data and Monte Carlo, for muons in dimuon events, for each of the variables used in the above muon identification cuts, see figure 5.1. When applied to muons, in dimuon events, the cuts had a selection efficiency of 84.2 $\pm$1.2% in good agreement with the Monte Carlo prediction of 85.6 $\pm$0.4%. Half of the loss in efficiency was due to the effect of inactive regions between neighbouring modules.

5.4 The Shadowing Problem

In the dense core of a hadronic jet, however, the situation is somewhat more complicated. When two TPC tracks are very close together the multiple scattering cones opened around their extrapolations may overlap. In this case the digital hits of one of the tracks may be mistakenly associated with both of them. If this happened one of

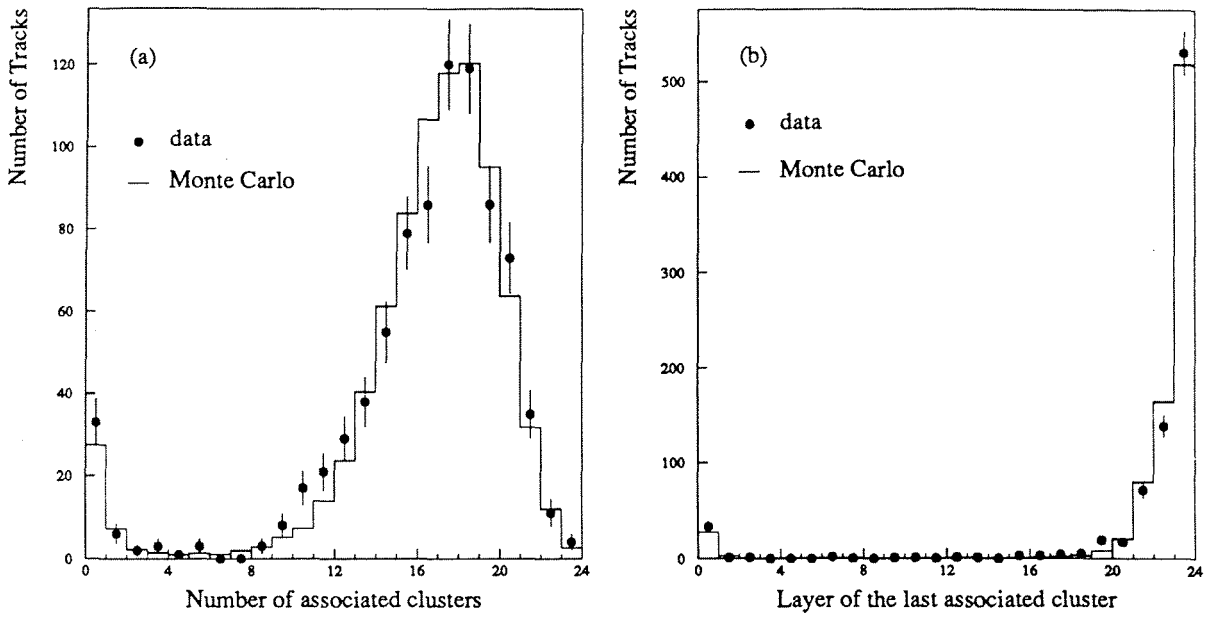

Figure 5.1: *Comparisons between data and tuned Monte Carlo simulation for (a) the number of associated clusters and (b) the HCAL layer of the last associated cluster for muons in dimuon events.*

the tracks was said to be *shadowing* the other. Before being treated shadowing affected 12% of all muon candidates with momentum over 3 GeV/c. When shadowing occurred the track which was deemed more likely to have caused the digital hits was selected while the other candidate was rejected. In order to make this choice the amount of lateral multiple scattering which a TPC track must have undergone to have caused its associated digital hits was measured. A variable α_{ms} was then defined as the ratio of this measured multiple scattering to the rms expected value. With this definition α_{ms} was Gaussianly distributed (mean 0, width 1) for real muons[2] but had a relatively flat distribution for shadowing hadrons. If one candidate had $|\alpha_{ms}| < 1$ while the other had $|\alpha_{ms}| > 2$, the former was identified as the muon. For the remaining cases the choice was based on the result of a maximum likelihood fit [35] performed between the digital hits and each of the candidate tracks. Monte Carlo studies suggested that a muon shadowed by a hadron was correctly chosen 82% of the time. The level of agree-

[2]At least for muons with momentum less than 20 GeV/c where the effects of multiple scattering dominated over measurement errors.

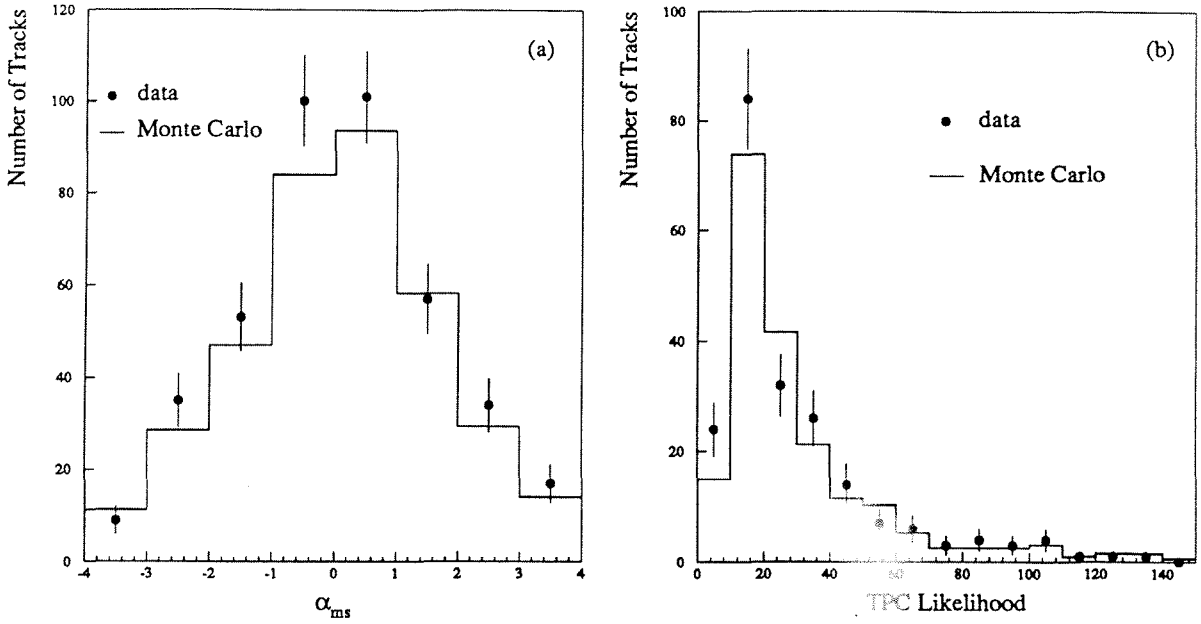

Figure 5.2: *Comparisons between data and Monte Carlo for (a) the average multiple scattering and (b) the computed TPC likelihood. This comparison was made for all muon candidates which were shadowed.*

ment between data and Monte Carlo for the distributions of the two variables used in making this choice, shown in figure 5.2, suggested that the relative error assigned to this prediction should be around 10%. This effect did not lead to any overall change in muon identification efficiency but simply meant that 2% of the final muon sample had the wrong associated momentum vector.

5.5 Backgrounds to the Prompt Muon Signal

The hadron contamination to the muon sample was due to three effects,

- pion or kaon decay in flight: where the muon faked a prompt muon,
- sail-through: a hadron which traversed the entire calorimeter without undergoing a strong interaction,
- punch-through: a strongly interacting hadron which produced one or more secondaries which left the calorimeter inside its multiple scattering cone.

Pion and kaon decays are very well understood and their effect can be accurately accounted for by the Monte Carlo. The decay muons had, in general, a much broader impact parameter[3] (d_0) distribution than the prompt ones. Thus rejecting all muon candidates with $|d_0| > 5$ mm kept over 99% of the prompt muons whilst rejecting 22% of the decay background. In the data the centroid of the beam axis was found to move around by up to 2 mm between different LEP fills. Before the d_0 cut could be applied to the data it was necessary to measure the position of the centroid of the beam axis for each LEP fill. This was obtained by looking, within a given fill, at the variation of the d_0 distribution (calculated with respect to the nominal beam axis) of *good* charged tracks with azimuthal angle. When the actual beam centroid was different from the nominal one the mean of this d_0 distribution plotted against azimuthal angle followed a sinusoidal distribution. The phase and amplitude of this sinusoidal variation was then used to calculate the real position of the beam centroid. Using this technique the average position of the centroid of the beam envelope was measured with an accuracy of around 50 μm.

The relative error on the Monte Carlo prediction of the residual decay background varies with

- the charged track multiplicity,
- the momentum distribution of these charged tracks,
- the ratio of kaons to pions observed in the data,

and was taken to be 15%.

A hadron *sailing* through the HCAL is indistinguishable from a muon and we rely on the Monte Carlo to simulate correctly this effect. The hadronic interaction probability is almost independent of momentum, for $p > 3$ GeV/c, but varies by up to 40% with particle type. The Monte Carlo prediction for the sail-through probability was tuned to the results of test-beam studies [36]. The test-beam measurements had a relative error of 20% and this was the error assigned to the simulation of the sail-through background.

[3]The impact parameter is the distance of closest approach of the track helix to the beam axis.

Punch-through background is however much more difficult to simulate as it involves a detailed modelling of the spatial development of hadronic showers. The predictions of the detector simulation have been shown to agree reasonably well with the level of punch-through background observed in test-beam data [36]. To reduce the effect of the uncertainty in this background to a minimum a further cut was made in order to suppress it. A search was made in a region ± 25 cm around the measured position of the muon candidate in the last ten planes of the HCAL for any evidence of excess activity which could be associated with a hadronic interaction. The size of the search region was chosen to be just large enough to contain the lateral spread of an average hadronic shower, as observed in the data. This search involved counting in this region

- the number of digital clusters (hits) associated with the given track $NCA(NHA)$,
- the number of digital clusters (hits) not associated with any track $NCU(NHU)$.

From these quantities a variable E_{xd} was defined, corresponding to an excess of digital energy in this region compared to that expected from a muon.

$$E_{xd} = \frac{NHA + NHU - NCA}{NCA}$$

The average value of E_{xd} was measured for dimuon events in both data and Monte Carlo and found to be 0.59 and 0.79 respectively. This difference was due to an overestimate of the induction effect between neighbouring tubes in the Monte Carlo. A muon candidate was rejected as being hadronic punch-through if it had both

- $NCU > 3$,
- and E_{xd} greater than twice the measured average for dimuons.

The cut was made on this combination of variables to avoid rejecting real muons due to either noise or delta ray production. It rejected 0.5% of the dimuons in both data and Monte Carlo. The majority of those rejected seemed to be caused by muon bremsstrahlung which should be less important for the lower momentum muons found in hadronic events. Monte Carlo studies showed that for inclusive muon candidates the cut rejected 50% of the punch-through background while keeping 99.5% of the muons.

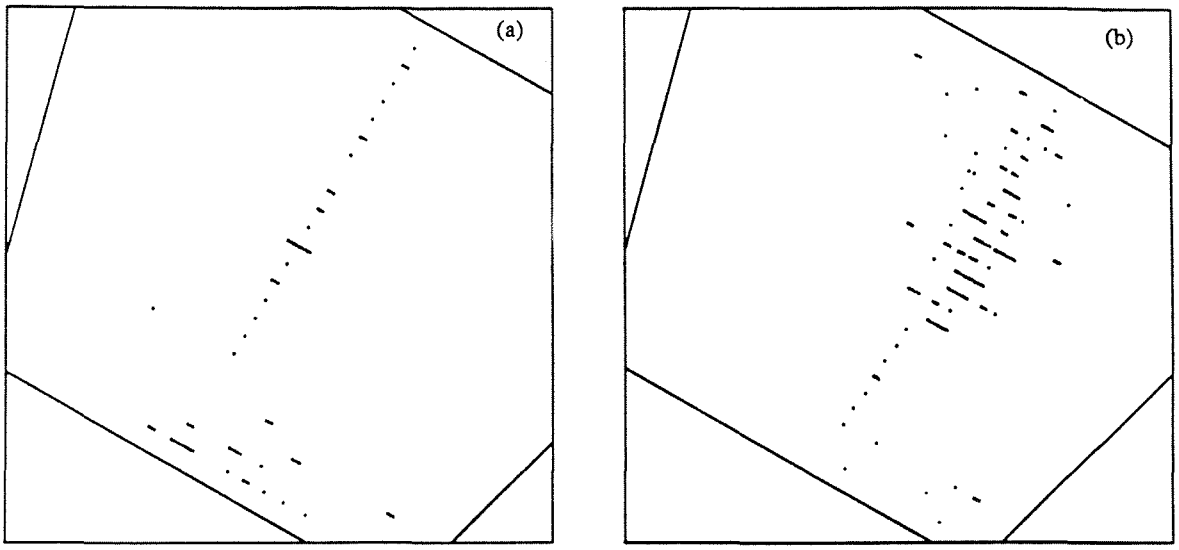

Figure 5.3: *Typical digital patterns associated with muon candidates which (a) pass and (b) fail the punch-through rejection cuts as observed in the data.*

Typical associated digital patterns for inclusive muon candidates which passed the other muon identification criteria but which then passed and failed the punch-through rejection cuts are shown in figure 5.3 (a) and (b) respectively. The residual punch-through contamination was around 4%; however the only way to estimate the error on this small background was by visual scanning of the events. The scan suggested that the remaining punch-through background was indeed quite well accounted for by the Monte Carlo. Since the results of a visual scan are very subjective a relative error of 60% was assigned to the Monte Carlo prediction.

5.6 Efficiency and Purity

With all the foregoing selection criteria applied[4] the ability of the Monte Carlo to reproduce accurately the background present in the data was verified using a pure sample of pions from K^0_s decays. In the data 0.9 $\pm$0.2% of these pions satisfied the cuts while the corresponding figure for the Monte Carlo was 0.85 $\pm$0.1%. However the relatively low average momentum of these pions meant that this cross-check was

[4]Except of course the d_0 cut.

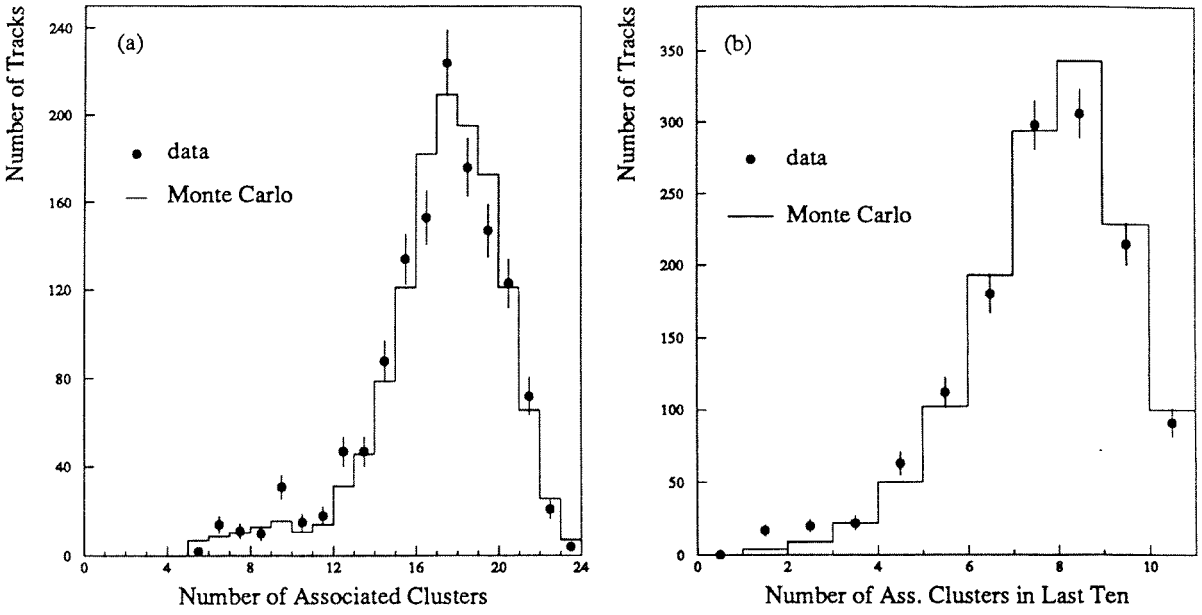

Figure 5.4: *Comparisons between data and tuned Monte Carlo simulation for (a) the number of associated clusters and (b) the number of associated clusters in the last 10 layers for inclusive muon candidates.*

primarily sensitive to the sail-through and decay backgrounds.

When all the background rejection cuts outlined were applied a reasonably good agreement was obtained between data and Monte Carlo for the variables used in the selection of inclusive muon candidates, figure 5.4.

The Monte Carlo was therefore used to predict the muon identification efficiency and hadron misidentification probability in $q\bar{q}$ events. The results obtained are given in table 5.1 in bins of p and $p_\perp$.

p	$p_\perp$	0.0-0.5	0.5-1.0	> 1.0
3-5	ϵ_μ	85±3	82±3	84±3
	ϵ_d	0.58±0.05	0.62±0.07	0.35±0.09
	ϵ_h	0.38±0.04	0.39±0.05	0.39±0.10
5-11	ϵ_μ	81±2	80±2	82±2
	ϵ_d	0.36±0.04	0.36±0.05	0.32±0.07
	ϵ_h	0.47±0.05	0.49±0.05	0.48±0.08
> 11	ϵ_μ	77±3	86±3	81±3
	ϵ_d	0.22±0.05	0.38±0.07	0.23±0.08
	ϵ_h	0.66±0.09	0.54±0.09	0.63±0.13

Table 5.1: *Muon identification efficiency (ϵ_μ), the contamination from $\pi^\pm$ and $K^\pm$ decays (ϵ_d) and the probability of misidentifying a hadron as a muon (ϵ_h). All numbers are given in percent, while p and $p_\perp$ are in units of* GeV/c.

Chapter 6

Electron Identification

6.1 The ALEPH Approach

In ALEPH the identification of inclusive electrons is achieved using both calorimetric information from the ECAL and rate of energy loss (dE/dx) measurements provided by the wire planes of the TPC. The two methods are independent and largely complementary, the former being most effective at high momentum (above 5 GeV/c) and the latter at low momentum.

The high granularity of the ECAL, in which each projective tower has a transverse size of approximately 3×3 cm^2 and is read out in three longitudinal stacks, enables good e–π separation in jets[1]. Electrons are identified by comparing the magnitude and profile of the energy deposition in the neighbourhood of an extrapolated track with respect to that expected for an electron.

The independence of the dE/dx measurement can be used to provide an accurate assessment of the proportion of hadrons passing the ECAL identification. When the dE/dx measurements are used in conjunction with the ECAL information a significant reduction in the level of hadron contamination can be achieved.

[1]The pad size (3×3 cm^2) is close to the lateral dimensions of an electromagnetic shower.

6.2 ECAL Identification

Each charged track with a momentum greater than 1 GeV/c is extrapolated up to its intersection with the ECAL taking into account the magnetic field, and then through the ECAL as though it were charge neutral. The intersection of this extrapolation with each of the three ECAL stacks is calculated and the energy deposited (E_{ij}) in the 4 storeys j nearest to this extrapolation is measured for each stack i. The centroid of each of these storeys (S_{ij}) is also recorded.

Test-beam data show that the variable

$$X = \frac{E_4}{p}, \quad \text{with} \quad E_4 = \sum_{i=1}^{3}\sum_{j=1}^{4} E_{ij},$$

is Gaussianly distributed for electrons of a given momentum. The mean $\langle X \rangle$ is 0.83 independent of entrance angle and momentum, for $p > 2$ GeV/c, while the variance $\sigma^2(X)$ is parameterized with respect to the resolution of the TPC momentum and the ECAL energy measurements according to test-beam results. Thus, for electrons, the variable

$$R_T = \frac{X - \langle X \rangle}{\sigma(X)}$$

is normally distributed with zero mean and unit variance.

Even for isolated particles, using just the 4 central storeys instead of the total associated energy, halves the level of hadron contamination without any measurable loss in electron identification efficiency. The reduction obtained reflects the lateral compactness of an electron's shower compared with that of a hadron. This momentum-energy balance criteria is ALEPH's most powerful tool for separating electrons from hadrons. However, further hadron rejection can be achieved by examining the longitudinal profile of the shower. On average an electron's shower will start much sooner after it enters the calorimeter and will also develop slightly faster than that of a hadron.

The inverse of the mean position of the longitudinal energy deposition (A) is defined as

$$A = \frac{E_4}{\sum_{i=1}^{3}\sum_{j=1}^{4} E_{ij}S_{ij}}$$

For isolated electrons of a given energy test-beam data show that A is Gaussianly distributed. The energy variation of $\langle A \rangle$ and $\sigma^2(A)$ is parameterized from test-beam measurements, giving a variable

$$R_L = \frac{A - \langle A \rangle}{\sigma(A)}$$

which for electrons is normally distributed with zero mean and unit variance.

A TPC track was identified as an ECAL electron candidate if it had

- $R_T > -3.0$,
- and $R_L > -3.0$,
- and $|\cos\theta| < 0.92$.

Tracks were explicitly excluded if they passed very close to a geometrically insensitive region between neighbouring modules. This excluded region accounted for 8% of the solid angle with $|\cos\theta| < 0.92$. No upper cut was made on either of the two estimators in order not to reject electrons which had overlapped with other calorimetric energy deposits.

From a scatter plot of R_T against R_L, figure 6.1, we can clearly distinguish an electron peak (centered on $R_T = R_L = 0.0$) nicely separated from the hadron background concentrated at low values of R_T and R_L. To examine the performance of these variables in the environment of hadronic jets a comparison was made of the R_T distributions, between data and Monte Carlo, after the R_L cut (for which the corresponding distributions agreed well) had been applied, figure 6.1. This figure showed that both had an obvious electron peak around 0.0. The Monte Carlo however overestimated the level of hadron background extending under this peak. This discrepancy was thought to be caused by a failure of the Monte Carlo to describe adequately the spatial development of hadronic showers.

The efficiency of this ECAL selection was checked using a pure sample of electrons, selected from photons converting in the material at the boundary between the ITC and

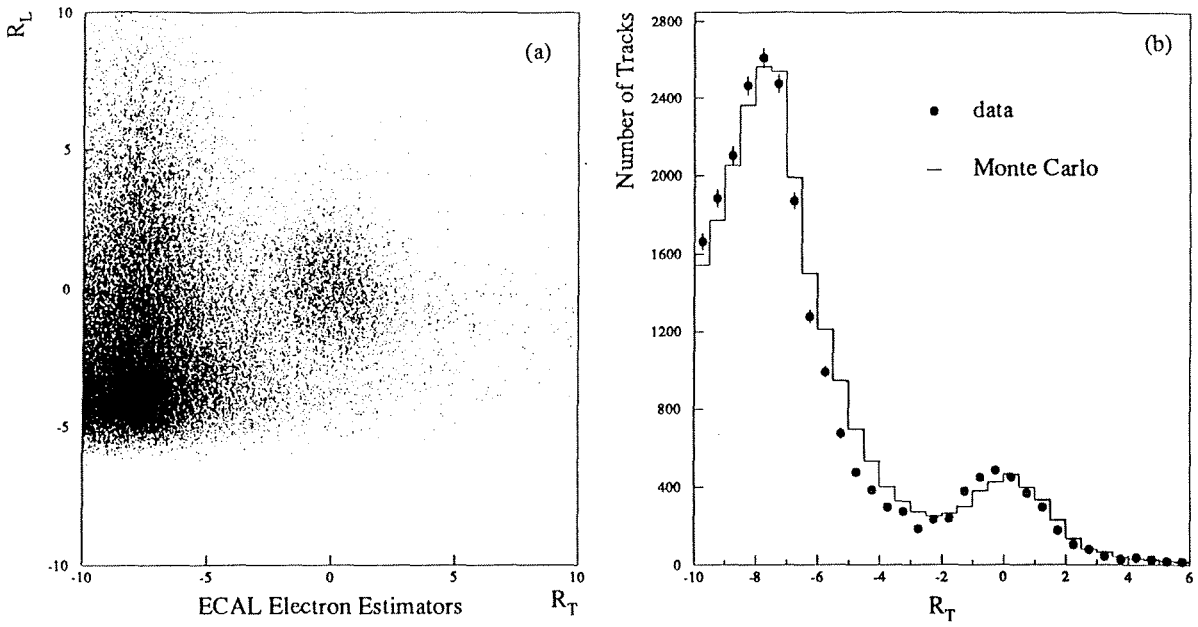

Figure 6.1: *(a) Scatter-plot of the two ECAL estimators R_T and R_L for tracks with $p > 3$ GeV/c in hadronic events. (b) Comparison between data and Monte Carlo for R_T after the cut on R_L had been applied.*

the TPC. The identification efficiency in the data of 94 $\pm$2% agreed within errors with a Monte Carlo prediction of 91 $\pm$1%. Unfortunately, due to limited statistics, it was not possible to use this technique to check the variation of the efficiency with p and $p_\perp$. There is, however, no reason to believe that the ability of the simulation to predict the efficiency would worsen at high values of p or $p_\perp$. The Monte Carlo prediction for the ECAL identification efficiency was used and assigned a relative systematic error of $\pm$3%.

6.3 TPC dE/dx Identification

The rate of energy loss by ionization (dE/dx) of a particle passing through a given medium depends only on its velocity. This dependence may be accurately parameterized using the relativistic Bethe-Bloch formula [37]. Thus for any given momentum a measurement of a particle's dE/dx allows a determination of its mass. Identification by dE/dx is particularly useful in selecting electrons, because of the relatively large mass

difference between them and all other charged particles.

The Bethe-Bloch formula predicts that a particle's dE/dx as a function of its velocity will fall to a minimum at $0.96c$ and then rise slowly before levelling off to form a plateau region. In the momentum region of interest electrons lie on that plateau whilst the much heavier hadrons are still on the relativistic rise. With increasing momentum the e–π separation obtainable decreases as the hadrons themselves approach the plateau region. In the TPC the dE/dx is measured by recording the pulse heights of the signals induced on the individual wire hits associated with each track. Up to 330 wire samples may be associated with any given track. The necessary requirement that any wire hits used should be isolated from the interference of nearby tracks will in general reduce this number and hence the accuracy obtainable on the dE/dx measurement.

The underlying processes involved in the ionization loss give a non-Gaussian distribution to the individual dE/dx losses produced when a particle crosses a very thin layer of low density material (such as the gas volume of the TPC). These fluctuations are caused by low probability collisions resulting in large energy loss. In fact the energy loss has an approximately Landau distribution having a relatively narrow and large peak at low values but a long tail. In order to minimize the effect of statistical fluctuations caused by this tail on the measured dE/dx the measured value used is taken to be the 60% truncated mean. The 60% truncated mean is formed by ordering the individual dE/dx wire samples by increasing pulse height and taking the average of the lowest 60% of them. Due to the large number of independent wire samples involved the Central Limit Theorem guarantees that the measured dE/dx (I) is Gaussianly distributed.

The measured dE/dx was calibrated to be uniform between the 36 different TPC sectors and over different run periods by using tracks selected from hadronic events. The variation of I with particle velocity was then parameterized from the data and normalized such that minimum ionizing pions had $I = 1.0$. With this normalization the expected dE/dx of an electron on the plateau $\langle I_e \rangle$ was 1.58. Figure 6.2 (a) shows the variation of the calibrated dE/dx with momentum for tracks from hadronic and leptonic Z decays. Also shown are parameterizations of the expected dE/dx ($\langle I \rangle$) for different particle types (e, μ, π, K, p) obtained by fitting the Bethe-Bloch formula to the data. The variance $\sigma^2(I)$ was parameterized from the data as a function of the number

of isolated wire samples used in the measurement. For an electron, in a hadronic event, with 330 isolated wire samples $\sigma(I)$ was measured to be 5.2%.

With the above definitions a variable R_I was defined as

$$R_I = \frac{I - \langle I_e \rangle}{\sigma(I)}$$

which for electrons was Gaussianly distributed with unit width and zero mean independent of momentum.

The hadron background present in the ECAL electron sample was significantly reduced by requiring each electron candidate to have

- at least 80 isolated wire samples,
- and $R_I > -2.5$.

Most of the additional inefficiency resulting from these cuts came from the requirement for each track to have 80 isolated wire samples. This inefficiency had a strong dependence on p and $p_\perp$. It was reasonably well accounted for by the Monte Carlo, however, small corrections were made, as a function of p and $p_\perp$ to the Monte Carlo predictions.

The method used in this analysis, which corrects the Monte Carlo predictions, differs from that used in the published ALEPH analysis [1]. In the published analysis it was assumed that prompt leptons and hadrons in the same p, $p_\perp$ bin had the same efficiency to have 80 isolated wire hits. The corresponding efficiency was then measured from the data by looking at all tracks except those coming from pair conversions. Subsequent Monte Carlo studies have, however, shown that the efficiency for prompt leptons is significantly higher than that for hadrons and that the technique used in the paper was therefore inappropriate. The higher efficiency for prompt leptons is probably related to the lower than average charged track multiplicity generated in semileptonic heavy flavour decays. Prompt leptons may therefore be somewhat more "isolated" than other particles.

The technique used in this analysis assumed that whatever was causing the difference in efficiency observed between data and Monte Carlo was independent of particle type. The spread in efficiency for particles from different sources was then taken from the

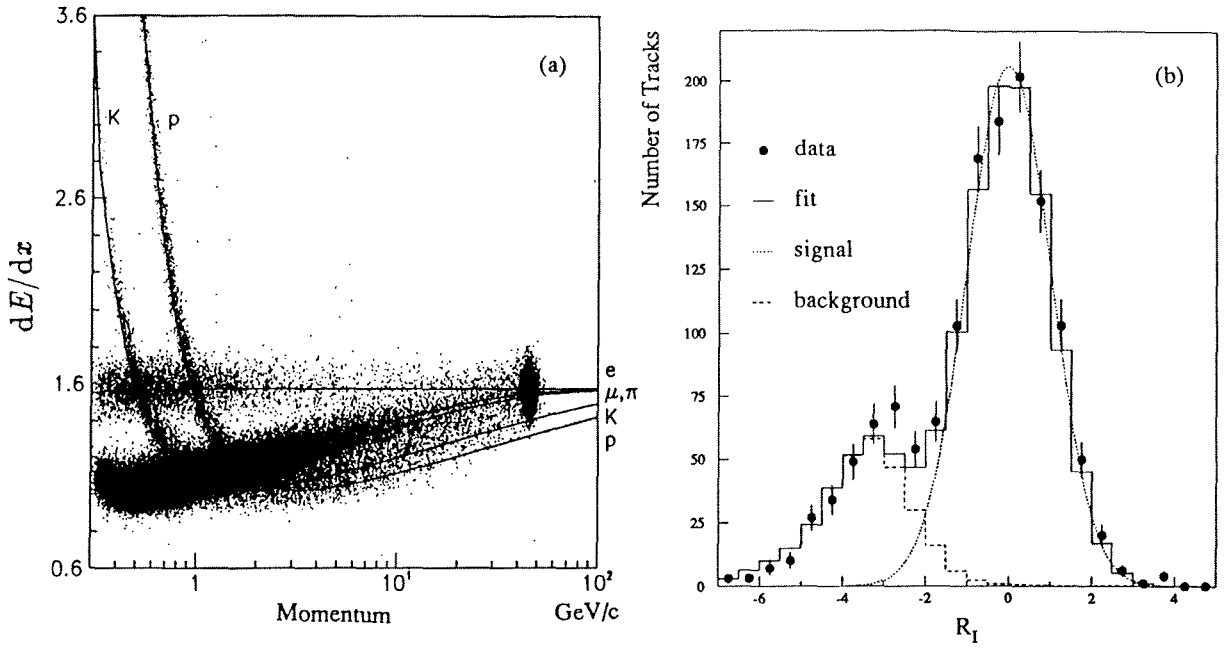

Figure 6.2: *(a) The measured dE/dx versus momentum for tracks in a sample of hadronic and leptonic Z decays. (b) The distribution of R_I for tracks, with* $3 < p < 5$ GeV/c, *passing the ECAL selection.*

Monte Carlo, after the average Monte Carlo efficiency, in each p, $p_\perp$ bin, was corrected to reproduce that observed in the data. The correction factors used were obtained as a function of p and $p_\perp$ by comparing the fraction of all tracks having 80 isolated wire samples between data and Monte Carlo. The efficiency for prompt electrons was then calculated by applying the correction factors obtained using all tracks to the Monte Carlo predictions for prompt electrons. The correction factors applied to the Monte Carlo prediction caused a decrease in efficiency by around 4% on average. This reduction is thought to be caused, at least partially, by the effect of dead wires which were not simulated by the Monte Carlo.

The residual inefficiency introduced by the requirement on R_I was only 0.5% and this was checked in the data by using electrons from pair conversions. Any non-Gaussian tails which the R_I distribution for electrons might have, would anyway be expected on the high side.

As well as allowing a reduction in the hadron background it was possible to use the dE/dx information to give a measurement of the residual hadron contamination, as a

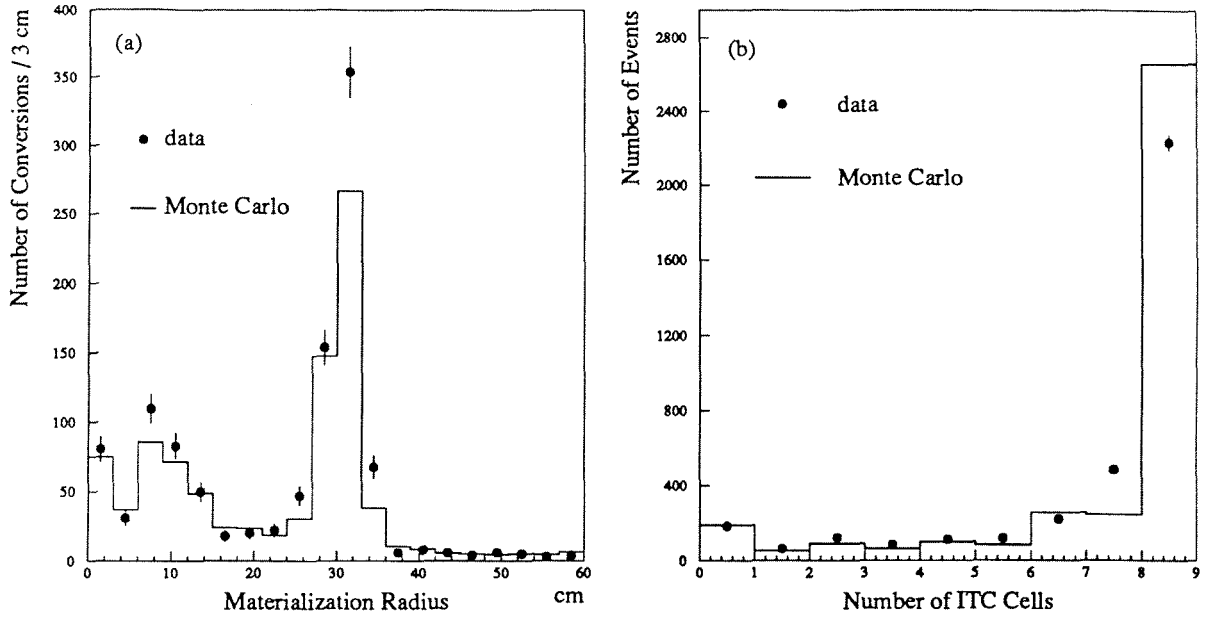

Figure 6.3: *Comparison between data and Monte Carlo for (a) the materialization radius of detected pair conversions and (b) the number of latched ITC cells associated with ECAL electron candidates.*

function of p and $p_\perp$, present in the final electron sample. In each p, $p_\perp$ bin the shape of the R_I distribution for "hadrons" was obtained by histogramming R_I for all tracks failing the ECAL electron identification criteria. The histogram obtained was then normalized to the R_I distribution of ECAL electron candidates in the region $R_I < -2.5$, where most of the tracks are "hadrons". The background in the final electron sample was predicted to be the area of the normalized histogram extending above $R_I > -2.5$. This technique assumed that the K–π ratio was not significantly affected by the ECAL identification cuts. The distribution of R_I for tracks, with $3 < p < 5$ GeV/c, passing the ECAL selection is shown in figure 6.2. The data are seen to be well described by a Gaussian, to describe the signal, plus a normalized background shape derived from the R_I of all tracks failing the ECAL identification. With the present statistics the systematic error on the prediction of the remaining background was dominated by the statistical error on the number of ECAL candidates failing the R_I cut.

6.4 Rejection of Background Electrons

There are two major sources of background from non-heavy flavour electrons: those produced by photons converting in the material of the detector and those from the Dalitz decay of a π^0 at the interaction point. When a massless photon converts it loses very little energy or momentum to the material and the e^+e^- pair produced will therefore, initially at least, have parallel trajectories.

Each electron candidate identified by the ECAL was paired with all tracks of opposite charge. The materialization point (M_P) of each pair was determined to be midway between the points on the two tracks where they were parallel (in the xy plane). An electron candidate was rejected if when so paired with another track

- their separation in the xy plane at their M_P was less than 1 cm,
- and their separation in z at their M_P was less than 1 cm,
- and the difference in θ between the two tracks was less than 0.007 radians.

An electron candidate was also rejected as coming from a pair conversion if

- either its distance of closest approach to the origin in the xy plane was more than 0.5 cm,
- or if more than 5 functional ITC cells through which it should have passed did not record the passage of any track.

A comparison between data and Monte Carlo for the radius of the materialization point of detected photon conversions is shown in figure 6.3. The shape and normalization of the two distributions agreed reasonably well except at the region between 30 and 34 cm which corresponded to conversions in the inner wall of the TPC. In this region the Monte Carlo underestimated the number of photon conversions by around 30 $\pm$6%. This was believed to be caused by an underestimate of the amount of material which GALEPH was given to simulate in that region. The number of ECAL candidates rejected by the cut on the number of associated ITC cells, figure 6.3, is 13 $\pm$3% greater

in the data than that predicted by the Monte Carlo, consistent with the above hypothesis. Overall the number of ECAL electron candidates rejected by the combination of the three cuts was 11 $\pm$3%.

The distribution in p and $p_\perp$ of the tracks rejected by these three cuts agreed well with that predicted by the Monte Carlo simulation. The pair conversion background was further suppressed by the requirement that any candidate have at least 80 isolated wire samples. The electron and positron from the photon conversions do not separate in θ and so have an abnormally low probability of having 80 isolated wire hits. The systematic error assigned to the Monte Carlo prediction of the remaining background for non-prompt electrons was 20% independent of p and $p_\perp$.

6.5 Efficiency and Purity

When all the above selection criteria had been applied the electron identification efficiency and hadron misidentification probability were calculated. The Monte Carlo was used to predict the efficiency of the ECAL and photon rejection cuts. The efficiency of the $\mathrm{d}E/\mathrm{d}x$ cuts was taken from the data as outlined above. The hadron misidentification probability was estimated from the data as outlined above. The results obtained are given in table 6.1 in bins of p and $p_\perp$.

p	$p_\perp$	0.0-0.5	0.5-1.0	> 1.0
3-5	ϵ_e	65±3	66±3	84±2
	ϵ_h	0.11±0.01	0.12±0.01	0.05±0.02
5-7	ϵ_e	56±4	59±4	74±3
	ϵ_h	0.19±0.04	0.17±0.04	0.24±0.07
7-11	ϵ_e	61±4	60±3	73±3
	ϵ_h	0.34±0.07	0.35±0.08	0.19±0.08
> 11	ϵ_e	19±1	41±2	61±3
	ϵ_h	0.27±0.11	0.54±0.15	0.16±0.12

Table 6.1: *The electron identification efficiency (ϵ_e) obtained after all cuts and the corresponding hadron misidentification probability (ϵ_h). All numbers are given in percent, while p and $p_\perp$ are in units of* GeV/c.

Chapter 7

Analysis of the Inclusive Lepton Spectra

Using the criteria outlined in the previous two chapters, inclusive lepton candidates were selected from a sample of hadronic Z decays collected at centre of mass energies between 88.3 and 94.3 GeV. From a sample of 21,384 hadronic Z decays 1,269 inclusive muon candidates were found with $p > 3$ GeV/c. Likewise 1,177 inclusive electron candidates with $p > 3$ GeV/c were obtained from a sample of 23,148 hadronic Z decays. The properties of these inclusive lepton candidates were compared with those selected from a sample of 72,000 Monte Carlo events. In the Monte Carlo the majority of these lepton candidates came from one of four types of semileptonic heavy flavour decay: namely $b \to lX, b \to \tau X \to lX, b \to cX \to lX$, or $c \to lX$ (where $l = e, \mu$). The Monte Carlo also predicted significant contributions from other sources, *e.g.* light hadron decay, hadron misidentification and, in the case of electrons, photon pair conversion. The Monte Carlo predictions for the relative contributions from the different types of heavy flavour decay depend on the relevant semileptonic branching fractions; those used are given in table 7.1.

The observed rate of production of inclusive leptons is sensitive to the $\Gamma(Z \to b\bar{b})$ partial width. The degree of sensitivity may be increased by selecting a region in which the dominant source of lepton production is semileptonic beauty decay. As outlined in section 1.6, the proportion of leptons coming from primary beauty decay

Branching Ratio		Reference
$b \rightarrow l\nu X$	0.102±0.010	[25]
$c \rightarrow l\nu X$	0.092±0.013	[21]
$b \rightarrow \tau\nu X$	0.05	[38]
$\tau \rightarrow l\bar{\nu}\nu$	0.175±0.004	[39]

Table 7.1: *Values for the semileptonic branching ratios used in the generation of the inclusive lepton spectra (l refers to electrons or muons).*

Region	$p_\perp > 0$		$p_\perp > 1$	
Source	μ	e	μ	e
$b \rightarrow l$	28	43	61	74
$b \rightarrow c \rightarrow l$	15	18	12	12
$c \rightarrow l$	15	20	9	9
background	42	19	18	5

Table 7.2: *The percentage of the inclusive muon and electron candidates coming from different sources both before and after a cut at* $p_\perp > 1$ GeV/c.

can be significantly enhanced by selecting only leptons which have a large transverse momentum with respect to their corresponding jet axis. The transverse momentum distributions of the selected muon and electron candidates is shown, for both data and Monte Carlo, in figures 7.1 (a) and (b) respectively. In these figures the Monte Carlo prediction is broken down into contributions from four distinct sources: primary beauty (including $b \rightarrow \tau X \rightarrow lX$), secondary charm, primary charm and background. From these spectra it is clear that a significant enhancement in the contribution from primary beauty decays can be achieved, with a reasonable efficiency, by requiring the lepton candidates to have $p_\perp > 1$ GeV/c. To quantify this statement the Monte Carlo predictions for the relative contributions from the four different sources are given in table 7.2, both before and after the $p_\perp > 1$ GeV/c cut was applied.

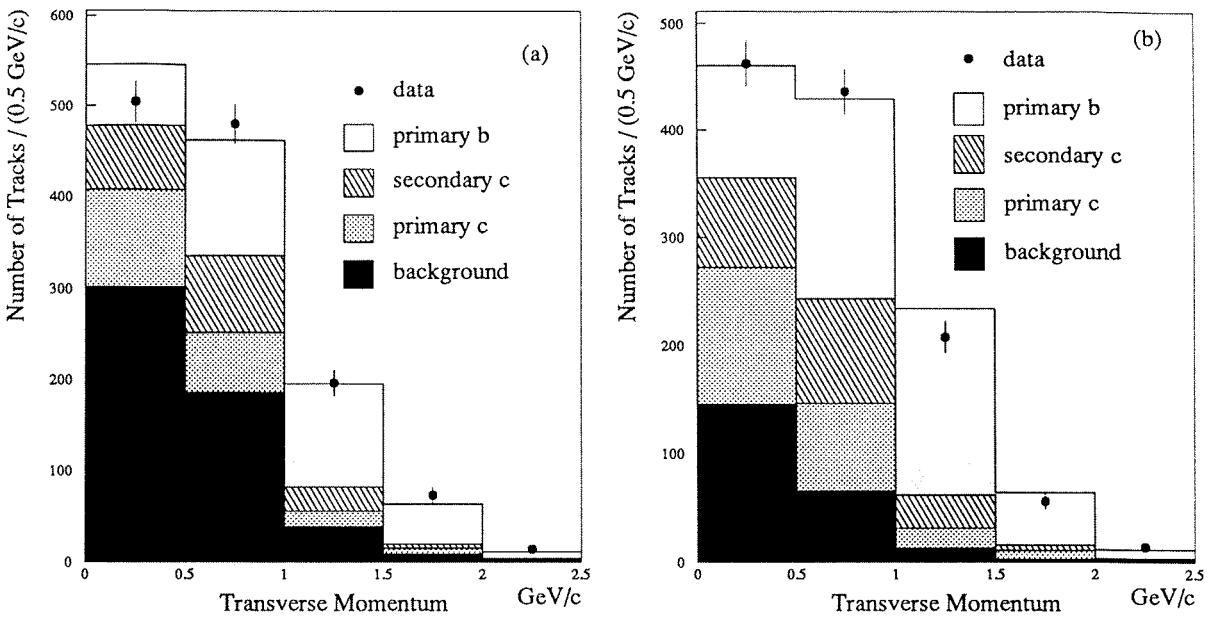

Figure 7.1: *Comparisons between data and Monte Carlo for the transverse momentum distributions of inclusive (a) muon and (b) electron candidates. The Monte Carlo predictions are decomposed into contributions from four distinct sources.*

Measurements of the $\Gamma(Z \rightarrow b\bar{b})$ width were obtained by counting the observed numbers of high $p_\perp$ lepton candidates and comparing them with Monte Carlo predictions for different quark flavours. In cases where a single event had more than one high $p_\perp$ lepton candidate all were retained. In the relevant event samples there were 285 muon and 279 electron candidates with $p_\perp > 1$ GeV/c. The momentum distributions of these high $p_\perp$ lepton candidates are shown in figure 7.2, together with the Monte Carlo predictions, decomposed into contributions from the four sources given above. The background contributions to these two samples were calculated, as outlined in the previous two chapters, and subtracted leaving 235 ± 17 muons and 262 ± 17 electrons from heavy flavour decays. The small contribution to these samples from primary charm decays was estimated by requiring

$$3\Gamma(Z \rightarrow b\bar{b}) + 2\Gamma(Z \rightarrow c\bar{c}) = \Gamma(Z \rightarrow q\bar{q})$$

where $\Gamma(Z \rightarrow q\bar{q})$ is the total hadronic width, which has been accurately measured by several experiments [14,40]. This constraint assumes that the Z boson couples equally to all quarks with the same weak hypercharge. Small corrections to the above formula,

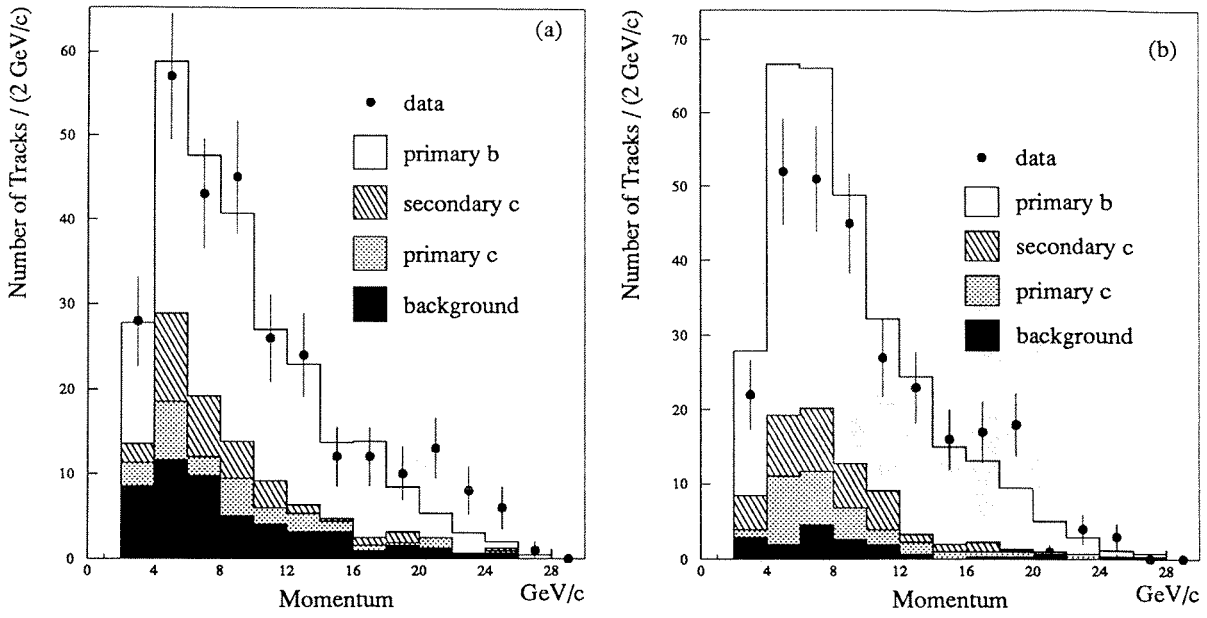

Figure 7.2: *Comparisons between data and Monte Carlo for the momentum distributions of the high $p_\perp$ (a) muon and (b) electron candidates.*

to take into account kinematical effects and uncertainties in the top quark mass, are unimportant given the size of the $c\bar{c}$ contribution and the experimental error obtainable on $\Gamma(Z \rightarrow b\bar{b})$. This constraint was used in preference to subtracting the $\Gamma(Z \rightarrow c\bar{c})$ width as predicted by the Standard Model.

Using the constraint the results obtained on the product of the $b\bar{b}$ branching fraction and the semileptonic branching ratio were

$$(\Gamma(Z \rightarrow b\bar{b})/\Gamma(Z \rightarrow q\bar{q})).Br(b \rightarrow \mu) = 0.0242 \pm 0.0026(stat) \pm 0.0018(syst),$$

and

$$(\Gamma(Z \rightarrow b\bar{b})/\Gamma(Z \rightarrow q\bar{q})).Br(b \rightarrow e) = 0.0187 \pm 0.0019(stat) \pm 0.0014(syst).$$

The systematic error quoted on each of these results was estimated by taking into consideration contributions from the following sources.

There were large contributions from uncertainties in the corresponding lepton identification efficiencies. The uncertainty in the muon identification efficiency was 3%. This was dominated by the effects of variations in the absolute normalization of the streamer tube efficiency map. The electron identification efficiency had a relative error

of 3.5%, determined primarily from the cross-check performed using electrons from pair conversions.

There were also sizable contributions from uncertainties in the amount of background predicted to be present in each of the two high $p_\perp$ lepton samples. For the muon sample the background prediction was taken from the Monte Carlo. The uncertainty in this prediction was calculated by summing in quadrature contributions from the different background sources weighted with the relative systematic errors (given in section 5.5). The effective uncertainty in the prediction of the background contamination was 18%. The background to the high $p_\perp$ electron sample came primarily from hadron misidentification. The uncertainty in the level of this background was obtained using the technique outlined in section 6.3. The corresponding uncertainty in the measured background level was 15%.

The remaining sources of systematic error were common to both the muon and electron channels. There was a systematic error arising from uncertainties in the simulation of the fragmentation of heavy flavour quarks. The effects of these uncertainties were studied by looking at the variation in the number of high $p_\perp$ leptons produced by reasonable changes in the ϵ_b parameter of the Peterson fragmentation function. This essentially corresponded to varying the hardness of the beauty quark fragmentation and hence the momentum of the leptons produced in beauty hadron decay. It was not possible to produce enough fully simulated events to allow this effect to be studied using the output of the reconstruction program. The study was therefore performed using generator simulation as outlined in section 4.4. The results obtained (figure 4.7) show that, within the formalism of the Peterson model, the effect of experimentally allowed variations[1] in the hardness of the beauty quark fragmentation results in a variation of the number of high $p_\perp$ leptons coming from beauty hadron decay of only 1%. If the $p_{\perp(j-l)}$ definition of transverse momentum had been used this variation would have risen to 5%. The shape of the momentum distributions of the high $p_\perp$ lepton candidates is sensitive to the hardness of the beauty quark fragmentation. The level of agreement between data and Monte Carlo for these distributions, figure 7.2, suggests

[1] ϵ_b was varied between 0.02 and 0.003 corresponding to the errors quoted on the experimental determination of $\langle X_b \rangle$ in [1,34].

Source	*Contribution*	
	μ	e
identification efficiency	0.009	0.009
background	0.012	0.003
fragmentation	0.002	
model dependence	0.009	

Table 7.3: *Contributions to the systematic error on the measurement of the product branching ratio* $(\Gamma(Z \rightarrow b\bar{b})/\Gamma(Z \rightarrow q\bar{q})).Br(b \rightarrow l)$ *coming from different sources.*

that the beauty quark fragmentation was adequately modelled by the Monte Carlo.

There was also a contribution to the systematic error resulting from the choice of spectator model used in the simulation of semileptonic beauty hadron decays. This model dependence arises because the shape of the lepton momentum distributions have only been measured [25] in the momentum region above 1.4 GeV/c. The $p_\perp$ of the lepton is also dependent upon the kinematics of the other charged tracks produced in the decay. The effect of these dependencies was investigated by tuning another two models (those of Bauer, Stech and Wirbel [41] and Grinstein, Isgur and Wise [42]) to reproduce accurately the CLEO data in the $p > 1.4$ GeV/c momentum region. Using generator simulation the variation in the number of high $p_\perp$ leptons obtained from the different models was found to be 5%.

The contribution to the systematic error arising from the inability of the event generator (JETSET) to describe perfectly the parton production, hadronization and particle decay processes was difficult to estimate. However the level of agreement obtained between data and JETSET simulation for a wide range of event shape variables was quite remarkable. It was therefore expected that the contribution to the systematic error from this source would be negligible. The contributions to the total systematic error from the various sources listed above are summarized in table 7.3.

The two measurements of the product branching ratio obtained above were compatible, within experimental errors, and were combined to give

$$(\Gamma(Z \rightarrow b\bar{b})/\Gamma(Z \rightarrow q\bar{q})).Br(b \rightarrow l) = 0.0206 \pm 0.0016(stat) \pm 0.0016(syst)$$

The $b\bar{b}$ production cross-section can only be extracted if the $Br(b \rightarrow l)$ branching ratio appropriate to LEP energies is known. Since the spectator model generally gives a good description of observed beauty meson decays, it was assumed that the average semileptonic branching fraction obtained for the mixture of beauty mesons produced at the $\Upsilon(4S)$ [25] was appropriate for the mixture of beauty hadrons produced at LEP. To account for possible deviations from this spectator model assumption the relative error on the measured branching fraction was increased from $\pm 7\%$ to $\pm 10\%$. This correction was derived by considering current limits on the ratio of the B^0 to B^+ lifetimes, expected rates of beauty baryon production, and estimated limits on the ratio of beauty baryon to beauty meson lifetimes (based on knowledge of the charm sector). Using the value of $Br(b \rightarrow l)$ of $10.3 \pm 1.0\%$ the fraction of hadronic Z decays which produced beauty quarks was measured to be

$$\Gamma(Z \rightarrow b\bar{b})/\Gamma(Z \rightarrow q\bar{q}) = 0.200 \pm 0.016(stat) \pm 0.026(syst).$$

and using the value of the total hadronic width measured in [14] we obtain

$$\Gamma(Z \rightarrow b\bar{b}) = 353 \pm 28(stat) \pm 46(syst)\,\mathrm{MeV/c}.$$

Chapter 8

Conclusions

Inclusive lepton production has been studied in a sample of around 25,000 hadronic Z decays observed by the ALEPH detector during the 1989 LEP running period. The momentum and transverse momentum distributions of these leptons were seen to be adequately described by a QCD based event generator which used spectator model predictions for the decay of heavy flavour hadrons. The product of the $b\bar{b}$ partial width and the average semileptonic branching fraction of beauty hadrons was measured from the production rate of high $p_\perp$ muons and electrons. The independent results from the muon and electron channels were consistent within experimental errors and were combined to give

$$(\Gamma(Z \to b\bar{b})/\Gamma(Z \to q\bar{q})).Br(b \to l) = 0.0206 \pm 0.0016(stat) \pm 0.0016(syst).$$

Using the average semileptonic branching ratio of beauty mesons measured at the $\Upsilon(4S)$ ($Br(b \to l) = 0.103 \pm 0.010$), the ratio of the $b\bar{b}$ to hadronic partial widths was measured to be

$$\Gamma(Z \to b\bar{b})/\Gamma(Z \to q\bar{q}) = 0.200 \pm 0.016(stat) \pm 0.026(syst)$$

in good agreement with the Standard Model prediction of 0.217[1]. The result obtained is also in good agreement with the published ALEPH result [1] and with measurements

[1]For $M_Z = 91.18\,\mathrm{GeV/c^2}$ [14], $\alpha_s = 0.12$ [15], $M_{top} = 150\,\mathrm{GeV/c^2}$, $M_{Higgs} = 100\,\mathrm{GeV/c^2}$.

obtained by other experiments [34,43,44]. With the exception of the DELPHI measurement, which used a boosted sphericity product analysis, the other experiments have used inclusive lepton production to tag the beauty quark events.

A more precise measurement of the $b\bar{b}$ partial width should soon be possible using a much larger hadronic event sample. As well as reducing the statistical error the increased sample size should allow a much better measurement of the background levels, giving a corresponding reduction in the overall systematic error.

For the next ALEPH measurement the efficiency of the muon identification will be increased by including the HCAL endcap region while the background contamination could be reduced by using information from the muon chambers. The muon chambers provide both a two dimensional space point and an exit angle for each muon candidate. This information may be used to substantially reduce the background coming from shadowing, light hadron decay and punch-through.

Recent Monte Carlo studies [45] have shown that significant reductions in the level of hadron background present in the ECAL electron sample may be obtained if the barycentre of the associated electromagnetic shower is required to match accurately the TPC track extrapolation. The level of background coming from pair conversions has, however, doubled after the installation of the entire Minivertex detector.

The systematic error could be further reduced if the separation between leptons from primary beauty decays and those from other sources could be increased. This will hopefully be achieved by including calorimetric information into the definition of the jet axes. The best separation obtained so far comes from using an *energy flow* analysis in which each *track* is a weighted superposition of contributions from the tracking, ECAL, and HCAL.

When all these improvements have been made the systematic error obtained on a measurement of the $b\bar{b}$ partial width will be dominated by the uncertainty in the experimental determination of the $Br(b \rightarrow l)$ branching ratio and in the shape of the corresponding lepton momentum spectrum. Both the CLEO and ARGUS experiments are currently undergoing hardware upgrades in preparation for further high luminosity runs. They should subsequently be able to improve their measurement of both the branching ratio and the shape of the lepton momentum distribution, at least in the

high momentum region. With a sample of 10^6 Z decays the LEP detectors should themselves be able to improve on the measurement of $Br(b \rightarrow l)$ branching ratio by analysing events with two high $p_\perp$ leptons in opposite hemispheres.

It remains an ongoing experimental challenge to measure the $\Gamma(Z \rightarrow b\bar{b})$ partial width with sufficient accuracy to be sensitive to top quark mass effects.

Bibliography

[1] D. Decamp *et al.* (ALEPH), Phys. Lett. **B244**, (1990) 551.

[2] N. Cabbibo, Phys. Rev. Lett. **10**, (1963) 531.
M. Kobayashi and T. Maskawa, Prog. Theor. Phys. **49**, (1973) 652.

[3] P.A.M. Dirac, Proc. Roy. Soc. London **A117**, (1928) 610.

[4] P.W. Higgs, Phys. Rev. Lett. **13**, (1964) 508.
P.W. Higgs, Phys. Rev. **145**, (1966) 1156.

[5] The concept of colour was first introduced to explain the Δ^{++} resonance. Further evidence came from measurements of $R = \Gamma(e^+e^- \rightarrow q\bar{q})\,/\Gamma(e^+e^- \rightarrow \mu^+\mu^-)$ Phys. Lett. **B204**, (1988) 119.

[6] S.L. Glashow, Nucl. Phys. **22**, (1961) 579.

[7] A. Salam and J. C. Ward, Phys. Lett. **13**, (1964) 168.

[8] S. Weinberg, Phys. Rev. Lett. **19**, (1967) 1264.
S. Weinberg, Phys. Rev. Lett. **27**, (1971) 1688.

[9] F.J. Hasert *et al.*, Phys. Lett. **46B**, (1973) 138.

[10] G. Arnison *et al.* (UA1), Phys. Lett. **122B**, (1983) 103.

[11] G. Arnison *et al.* (UA1), Phys. Lett. **126B**, (1983) 398.

[12] R.P. Feynman, Phys. Rev. **76**, (1949) 749-769.

[13] Z Physics at LEP 1 - Vol:1, CERN 89-08, 268-271.

[14] D. Decamp *et al.* (ALEPH), Z. Phys. **C48**, (1990) 365.

[15] D. Decamp *et al.* (ALEPH), preprint CERN EP-89-139.

[16] T. Sjöstrand and M. Bengtsson, Comp. Phys. Com. **43**, (1987) 367.

[17] A. Petersen *et al.* (MARK II), Phys. Rev. **D37**, (1988) 1.
W. Braunschweig *et al.* (TASSO), Z. Phys. **C41**, (1988) 359.
W. Bartel *et al.* (JADE), Z. Phys. **C33**, (1986) 23.
Y. Li *et al.* (AMY), *Multihadronic Event Properties in* e^+e^- *Annihilation at* $\sqrt{s}$ 52 *to* 57 GeV/c. Submitted to the XIV International Symposium on Lepton and Photon Interactions, Stanford, CA (1989).

[18] Z Physics at LEP 1 - Vol:3, CERN 89-08, 143-340.

[19] J.E. Campagne and R. Zitoun, Z. Phys. **C43**, (1989) 469.

[20] B. Andersson *et al.*, Phys. Rep. **97(2,3)**, (1983) 31-171.

[21] B. Adeva *et al.* (MARK J), Phys. Rev. Lett. **51**, (1983) 443.
H. J. Berend *et al.* (CELLO), Z. Phys. **C19**, (1983) 291.
B. Fernandez *et al.* (MAC), Phys. Rev. Lett. **50**, (1983) 2054.
M. Althoff *et al.* (TASSO), Z. Phys. **C22**, (1984) 219.
H. Aihara *et al.* (TPC), Phys. Rev. **D31**, (1985) 2719.
T. Pal *et al.* (DELCO), Phys. Rev. **D33**, (1986) 2708.
W. Bartel *et al.* (JADE), Z. Phys. **C33**, (1987) 339.
R. Ong *et al.* (MARK 2), Phys. Rev. Lett. **60**, (1988) 2587.

[22] C. Peterson *et al.*, Phys. Rev. **D27**, (1983) 105.

[23] J.G. Kröner and G.A. Schuler, Z. Phys. **C38**, (1988) 515-518.

[24] See discussion in S. Dugeay and P. Henrard, ALEPH-88-82 (unpublished).

[25] H. Albrecht *et al.* (ARGUS), preprint DESY 90-088.
J. Alexander, in: Les Recontres de Physique de la Vallee d'Aosta (La Thuile, March 1990): result to be published in Phys. Rev. D.

[26] R. Fulton *et al.* (CLEO), Phys. Rev. Lett. **64**, (1990) 16.
H. Albrecht *et al.* (ARGUS), preprint DESY 89-152.

[27] W. Bartel *et al.* (JADE), Z. Phys. **C33**, (1987) 339-349.

[28] *Large Electron-Positron storage ring, Technical Notebook*, CERN Publications, European Laboratory for Particle Physics,1211 Geneva 23, Switzerland, Nov. 1989.

[29] D. Decamp *et al.* (ALEPH), Nucl. Inst. Meth. **A294**, (1990) 121-178.

[30] J. Jowett, preprint CERN LEP-TH-87-17.

[31] R.E. Kalman, J. Basic Eng., **82**, (1960) 35.
R.E. Kalman and R.S. Busy, J. Basic Eng., **83**, (1961) 95.
P. Billior, Nucl. Inst. Meth., **A225** (1984), 352.

[32] W. Wiedenmann, IEEE Nuclear Science Symposium, Arlignton, VA, USA (1990).

[33] W. Bartel *et al.* (JADE), Z. Phys. **C33**, (1986) 23.
S. Bethke, Habilitationschrift, University of Heidelberg(1987)(unpublished).

[34] B. Adeva *et al.* (L3), Phys. Lett. **B241**, (1990) 416.

[35] L. Passalacqua, Tesi di Laurea in Fisica, Universita' di Roma "La Sapienza", Rome, Italy, (1990)

[36] M. de Palma, ALEPH-89-157 (unpublished).

[37] H.A. Bethe and J.A. Ashkin, Exptl. Nucl. Phys. **1**, (1953) 166.

[38] C. Quigg and J.L. Rosner, Phys. Rev. **D19**, (1979) 1532.

[39] G.P. Yost *et al.*, Phys. Lett. **B204**, (1988) 13.

[40] B. Adeva *et al.* (L3), Phys. Lett. **B231**, (1989) 509.
P. Aarnio *et al.* (DELPHI), Phys. Lett. **B231**, (1989) 539.
M.Z. Akrawy *et al.* (OPAL), Phys. Lett. **B231**, (1989) 530.

[41] M. Wirbel, B. Stech and M. Bauer, Z. Phys. **C29**, (1985) 637.

[42] B. Grinstein M.B. Wise and N. Isgur, Phys. Rev. Lett. **56**, (1986) 258.

[43] J. F. Kral *et al.* (MARK II), Phys. Rev. Lett. **64**, (1990) 1211.

[44] P. Abreu *et al.* (DELPHI), preprint CERN PPE-90-118.

[45] M. Talby, private communication.